TUDelft

Delft University of Technology

Storing CO$_2$ in geothermal reservoir rocks from the Kizildere field, Turkey
Combined stress, temperature, and pore fluid dependence of seismic properties

Janssen, Martijn T.G.; Draganov, Deyan; Barnhoorn, Auke; Wolf, Karl Heinz A.A.

Important note
To cite this publication, please use the final published version (if applicable).
Please check the document version above.

Storing CO_2 in geothermal reservoir rocks from the Kizildere field, Turkey: Combined stress, temperature, and pore fluid dependence of seismic properties

Martijn T.G. Janssen [*], Deyan Draganov, Auke Barnhoorn, Karl-Heinz A.A. Wolf

Department of Geoscience and Engineering, Faculty of Civil Engineering and Geosciences, Delft University of Technology, Stevinweg 1, Delft 2628 CN, the Netherlands

ABSTRACT

As part of a seismic monitoring project in a geothermal field, where the feasibility of re-injection and storage of produced CO_2 is being investigated, a P- and S-wave seismic velocity characterisation study was carried out. The effect of axial and radial (up to 42 MPa) stress, pore pressure (up to 17 MPa), pore fluid (100% brine or supercritical CO_2) and temperature (21–100 °C) on seismic properties were studied in the laboratory for the two main reservoir formations at the Kızıldere geothermal reservoir. Each (un)confined compressive strength test performed revealed a similar trend: rapidly increasing velocity at low stresses followed by a more moderate increase at higher stresses. The data implied that the stress-dependency of the velocity increased with temperature. Increasing temperatures resulted in decreasing P-wave velocities due to mineral thermal expansion. This temperature-dependency increased with reducing stress levels. The S-wave velocity seems to be more sensitive to changes in pore pressure than the P-wave velocity. On the other hand, the S-wave velocity is less affected by an increasing axial stress compared to the P-wave velocity. By performing multiple nonlinear regression on the velocity dataset, related to a brine-saturated fractured marble, second-degree polynomial trends were found for the P- and S-wave velocity, as a function of temperature, axial stress, and pore pressure, that can potentially be used for predicting velocities at Kızıldere, or other similar, geothermal site(s). For distinguishing between a 100% brine-saturated versus a fully supercritical CO_2-saturated fracture, the arrival times of the first arrivals were too close to each other to allow their utilization. The fracture aperture was too small compared to the wavelength of the source signal. However, differences in P- and S-wave amplitudes of the first arrivals were seen, where the supercritical CO_2-saturated crack revealed consistently lower peak and trough amplitudes compared to the brine-saturated scenario.

1. Introduction

Due to a combined effect of population and economic growth, the global energy demand is expected to increase significantly during the next decades (Zohuri, 2020; IEA 2021; Soltani et al., 2021). For mitigating climate change, and thus for meeting the Net Zero Emissions by 2050 Scenario, part of the expected growth in the energy demand might be supplied by non-fossil-based energy resources such as geothermal energy. This source of renewable energy originates from the heat flux from the earth's core, allowing the production of hot water and steam from geothermal reservoirs for the aid of electricity generation and heating (Barbier, 2002; IEA 2021; Soltani et al., 2021). In 2020, the generation of electricity utilizing geothermal energy increased with an estimated 2%, corresponding to more than 200 MW, reaching a total installed capacity of approximately 15,800 MW globally (IEA, 2021).

Turkey has seen a significant growth in its installed geothermal capacity over the past five years, reaching a total of approximately 1710 MW at the end of 2021 (IEA, 2021). The majority of the installed capacity in Turkey comes from geothermal power plants operating along the Büyük Menderes Graben (Kaygusuz et al., 2019; Yamanlar et al., 2020; Janssen et al., 2021; Ozcelik, 2022). Practically all geothermal production wells in the Büyük Menderes Graben produce from carbonate reservoir rocks, leading directly to considerable amounts of dissolved carbon dioxide (CO_2) in the produced geothermal fluids (Akin et al. 2020; Bustaffa et al., 2020; Parlaktuna et al., 2021; Ozcelik, 2022). At the surface facilities, the produced non-condensable CO_2 is vented to

---

the atmosphere whereas the CO_2-depleted geothermal fluid is re-injected into the reservoir.

The work presented here is part of the ACT2 CCS SUCCEED project whose goal is to investigate the viability of re-injecting produced CO_2 back into a geothermal field, for permanent storage and enhancing reservoir pressure, instead of emitting it to the atmosphere. More detailed information on the SUCCEED project is given elsewhere (Janssen et al., 2021; Parlaktuna et al., 2021).

This study focusses on one particular active geothermal power generation site within the Büyük Menderes Graben system: Kızıldere. Here, reservoir temperatures up to 240 °C are found, allowing for exploitation for electricity production (Gokcen et al., 2004; Güleç and Hilton, 2016). Existing infrastructure will be used to re-inject produced CO_2, in a supercritical state, into the carbonate reservoir.

The work we present below covers a detailed, comprehensive, laboratory investigation of the combined effect of stress, temperature, pore fluid type, and pore pressure on the seismic response of two individual reservoir formations at Kızıldere. Experimental studies of the dependence of seismic velocities on temperature (Timur, 1977; Kern, 1978; Kern et al., 2001; Punturo et al., 2005; Scheu et al., 2006; Yavuz et al., 2010; Jaya et al., 2010; Haep et al. 2013; Qi et al., 2021), stress and pore pressure (Wyllie et al., 1958; Podio-Lucioni, 1968; Nur and Simmons, 1969; Prasad and Manghnani, 1997; Darot and Reuschlé, 2000; King, 2009; Qi et al., 2021), and pore fluid type (Mavko and Mukerji, 1998; Shi et al., 2007; Njiekak et al., 2013) are available in existing literature. However, the bulk of aforementioned studies were conducted under extremely high pressures (up to several hundreds of MPa) and temperatures (up to 1000 °C, in steps of 100 °C), or, if a more realistic (for geothermal systems) temperature and stress range was used, do not involve CO_2 as a pore fluid.

This work serves as a full extension of our earlier experimental work on stress-dependency of seismic velocities for a wide range of dry sedimentary and metamorphic rocks that form the different reservoir and caprock formations at Kızıldere (Janssen et al., 2021). Here, we present an extensive, well-controlled, and detailed laboratory study of the combined stress (up to 42 MPa), temperature (up to 100 ± 1 °C), pore pressure (up to 17 MPa), and pore fluid (brine or supercritical CO_2) dependence of the seismic properties in the two main metamorphic reservoir formations that make up the Kızıldere geothermal system: marble and calcschist. Using the sourced reference samples from the area around Kızıldere, active-source acoustic transmission measurements, at field-representative reservoir conditions, are performed for obtaining a seismic-response characterisation tailored for the Kızıldere geothermal reservoir.

2. Materials and methods

2.1. Sample collection and core preparation

The Kızıldere geothermal field is located in the southwest of Turkey and exhibits temperatures of up to 240 °C at depths below 1200 m (Garg et al., 2015; Halaçoglu et al. 2018). The produced geothermal fluid is of meteoric origin that gets heated from circular flow within existing fractures in the high heat-flow regime. A more detailed description of the geothermal site, and a conceptual model of the Kızıldere field, is shown in Janssen et al. (2021) and Parlaktuna et al. (2021).

Marble and calcschist rock samples were collected from various outcrops in the area around the Kızıldere geothermal site. They represent the main reservoir formations within the Menderes Massive, which forms the second reservoir at Kızıldere (Janssen et al., 2021). From the gathered reservoir rock samples, multiple cores were drilled perpendicular to any potential layering. Average core length and diameter equal 49.1 ± 0.3 mm and 25.3 ± 0.1 mm, respectively. After drilling them, they were placed in an oven to dry at 60 ± 1 °C for 24 h. Subsequently, the porosity, matrix density, and bulk density of each of the cores were measured with an Ultra Pycnometer 1000 (Quantachrome

Corporation™). Table 1 gives an overview of the physical properties of the core samples used in this study.

2.2. Thin sections, XRD, XRF, and micro-CT scan analyses

For texture analyses and mineralogical and phase determination, 30 µm thin sections were prepared and combined with X-ray diffraction (XRD) and fluorescence (XRF) analyses on grounded and sieved material from the same marble block (Fig. 1-B) where Marble-1 and Marble-frac (Table 1) were drilled from. A Leitz™ Laborlux 11 pol S. microscope (Ernst Leitz GmbH) was used to obtain a petrographic and mineralogic overview of the thin section, as well as a texture description. Random point-counting was used for the determination of the mineral composition and porosity. A Bruker™ D8 Advance (CuKα radiation) diffractometer, with Bragg-Brentano geometry and position-sensitive Lynxeye detector, was used for a bulk mineral phase determination (i.e., XRD analysis). The bulk element oxide composition, i.e., XRF analysis, was obtained with a Panalytical™ Axios Max WD-XRF spectrometer. Volumetric texture heterogeneity of a cored marble sample (length and diameter of 75.4 and 36.6 mm, respectively), that was drilled from the same block as Marble-1 and Marble-frac in Table 1, was visualized, based on density variation, and quantified with an X-ray micro-computed-tomography (micro-CT) scanner (Phoenix Nanotom 180NF). Scans were taken using an X-ray tube with 160 kV voltage and a current of 240 µA, yielding a voxel size of $0.06 \times 0.06 \times 0.06$ mm^3. The image batches were analysed and visualized by using ImageJ software. Note that the thin section, XRD, XRF, and micro-CT scan analyses were performed on marble material, representative for Marble-1 and Marble-frac in Table 1, only.

After the marble thin section was prepared, it was subsequently used to assess its mineralogy and to calculate the 2D permeability according to the 2D Carman-Kozeny equation (Kozeny, 1927; Carman, 1937; Coskun and Wardlaw, 1993). For 2D permeability estimation, spatial characteristics of the porosity, i.e., area and perimeter distribution, were used. Results imply that the presence of fractures increase the 2D permeability by approximately a factor 20: from 0.1 Darcy for the matrix permeability only to 2.2 Darcy for the matrix including the open fracture. This is in line with the observation that geothermal deployment at Kızıldere is mainly depending on fluid flow through networks of continuously developing tectonic (micro-)fractures (Garg et al., 2015; Halaçoglu et al. 2018). Note that the presented 2D permeability is likely to be overestimated due to preparation damage and a stress-free matrix. In terms of mineralogy, the thin section analysis indicated that the Kızıldere marble consists mainly (circa 99 area-%) of fully recrystallized calcite and dolomite, and accessory clay, oxides, and sulphides. An example of parallel and crossed nicols are shown in the top and bottom part of Fig. 1-D, respectively.

Powdered marble material was sourced from the two areas indicated as 'red' and 'white' marble in Fig. 1-A (which presents a surface area present on the large-scale marble block shown in Fig. 1-B). It was used for the XRD and XRF analyses. The synthetical XRF analysis show that the chemical composition of the 'white marble', i.e., the marble sample without fracture, consists of >97 wt% calcium oxide (CaO) and >1wt% magnesium oxide (MgO). The 'red marble', i.e., the sample containing a

Table 1
Properties of the marble and calcschist cores used.

Type	Experiment Calcschist	Marble	Marble
Code	TD13-CS-4	Marble-1	Marble-frac
Length (mm)	48.8 ± 0.1	49.0 ± 0.1	49.4 ± 0.1
Diameter (mm)	25.3 ± 0.1	25.2 ± 0.1	25.3 ± 0.1
Porosity (%)	1.79 ± 0.22	0.59 ± 0.13	3.29 ± 0.08
Pore Volume (mm^3)	439 ± 58	144 ± 34	817 ± 28
Matrix density (g/cm^3)	2.73 ± 0.01	2.71 ± 0.01	2.71 ± 0.01
Bulk density (g/cm^3)	2.69 ± 0.03	2.70 ± 0.03	2.61 ± 0.02
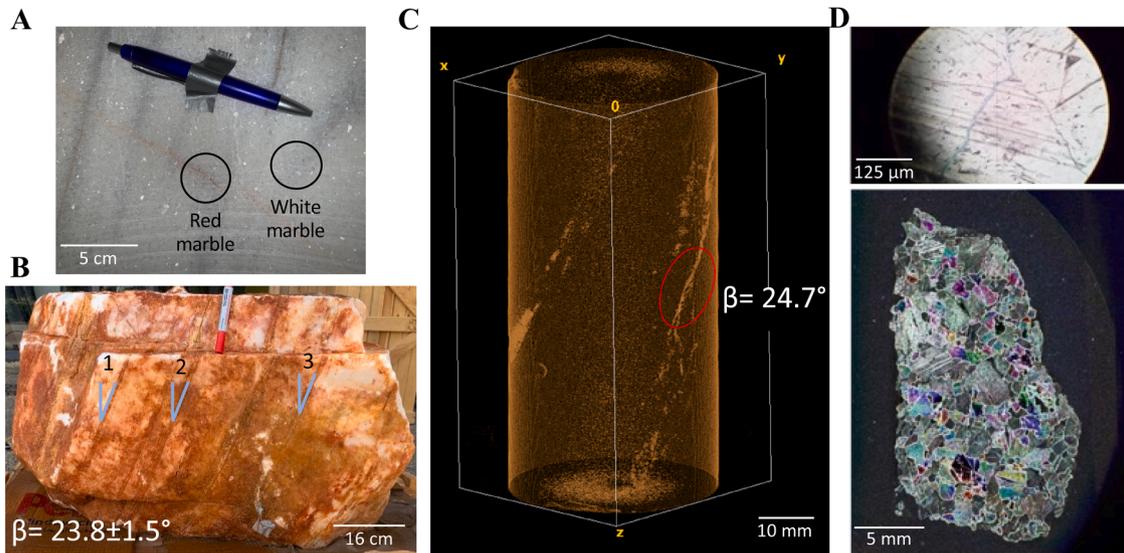
Fig. 1. (A) Image of the marble surface indicating the two samples – red (including crack with red-filled material) and white (without the presence of any crack) marble – used for performing the XRD and XRF analyses. (B) Large marble block from which samples were taken for the aid of thin section, XRD, XRF, and micro-CT scan analyses. Note the field-representative fracture pattern with an averaged fracture angle β of 23.8 ± 1.5° (based on three individual measurements). (C) Post-processed micro-CT image of a marble core (length and diameter of 75.4 and 36.6 mm, respectively) drilled from the large block shown in (B). The image was constructed following a threshold operation, highlighting any fractures present. Note the β of roughly 24.7°, which corresponds to the large-scale angle analysis done in (B). (D) Parallel (top) and crossed (bottom) nicols for a marble thin section. Note the interfaces, between larger calcite mineral grains, with blue intergranular porosity (top).

fracture with red matter, contains >91 wt% CaO and >3 wt% silicon dioxide (SiO_2). Additionally, the XRF data show that the 'red marble' contains more iron compared to the 'white marble'. The XRD analysis shows that both the 'red marble' and 'white marble' samples mainly contain calcite with some dolomite compounds, similar to the observations made during thin section analysis.

The large marble block (Fig. 1-B) shows the existing, field-type, natural fracture network of which most former fractures are recrystallized and covered by new fractures. Fracture angles (β) were calculated for three individual fractures (Fig. 1-B), yielding an averaged β of 23.8 ± 1.5°. Next, micro-CT scans were performed on a marble sample,

drilled from the large block (Fig. 1-B), in order to characterise the natural fracture network on core-scale (cm), and subsequently compare it to the observations done on the large-scale block (m). Fig. 1-C presents a 3D view of the scanned marble sample. Thresholding on grey values was done, yielding a volume highlighting any fracture pattern that may be present. Calculations revealed a β of 24.7°, which falls in the range of angles identified on the large-scale block.

2.3. Experimental apparatus

Experiments performed include active-source acoustic-assisted
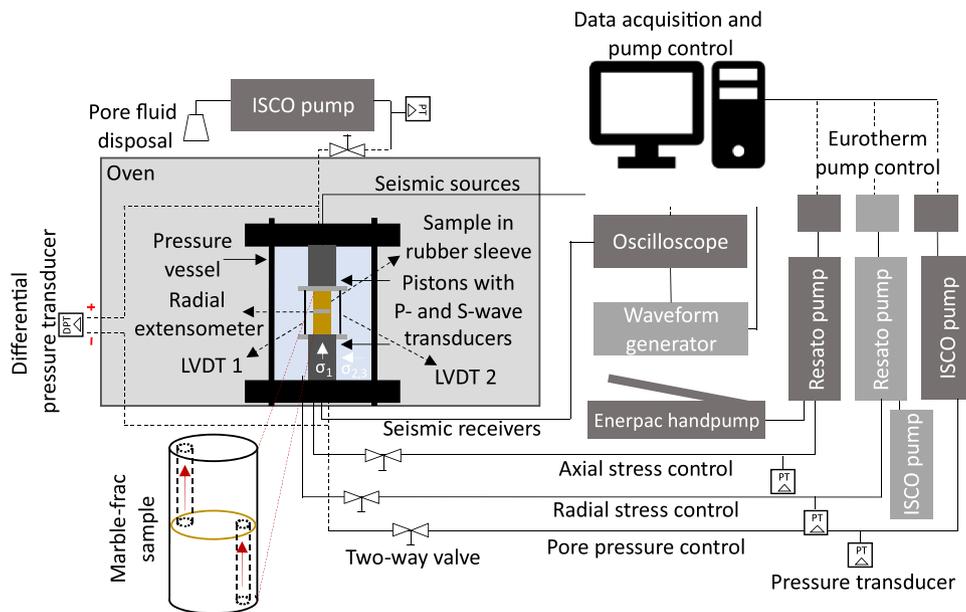
Fig. 2. Schematic of the experimental set-up. In the bottom left a sketch of the artificial fractured marble sample (Marble-frac) is shown. It was created by cutting the sample in two, creating a fracture plane presented in brown. Moreover, in- and outlet holes were drilled from each side of the core sample (red arrows displays the flow path).

unconfined compressive strength (UCS) tests, where only axial stress (σ_1) without additional radial stress ($\sigma_2 = \sigma_3$) was imposed on the system, and confined compressive strength (CCS) experiments, where both σ_1 and $\sigma_2 (= \sigma_3)$ were induced on the sample. Fig. 2 presents a schematic of the experimental set-up used for performing the acoustic-assisted UCS and CCS experiments. For all experimental series, first the rock samples were placed inside a rubber sleeve before being positioned between two pistons within a pressure vessel (Fig. 2). With the sample in place, the pressure vessel was closed using multiple metal rods, and subsequently filled with a high-performance hydraulic oil (Shell Tellus S2 VX 46). The hydraulic oil was pressure-controlled by a Resato pump, which was filled by a separate ISCO pump. In this way, $\sigma_2 (= \sigma_3)$ was imposed on the sample in a controlled manner over the course of an experiment. The same oil was used for providing, and controlling, σ_1. The hydraulic oil was inserted in a Resato pump utilizing an Enerpac handpump. Afterwards, the Resato pump, again in a pressure-controlled format, injected the oil into the bottom piston where a hydraulic ram was used for regulating σ_1. Two separate linear variable-displacement transformers (LVDTs) and a radial extensometer were utilized for recording the axial and radial strain, respectively. For three experiments with pore fluid (3-CCS-c, 4-CCS-a, and 4-CCS-b in Table 2 – will be introduced in Section 2.4), a separate ISCO pump was used for controlling the pore pressure (P_p). For these experiments, a marble sample (Marble-frac in Table 1) that contains an artificial horizontal fracture (covering the entire cross-sectional area), was used. The fracture was formed by cutting the sample halfway perpendicular to its length axis. Inlet/outlet holes (3.4 ± 0.1

Table 2
Overview of the experimental series performed in this study.

Experiment	Sample	Radial stress (MPa) ($\sigma_2 = \sigma_3$)	Axial stress (MPa) (σ_1)	Pore fluid pressure (MPa)[b]	Temperature (°C)[a]
1-UCS	a-Marble-1	0.08 ± 0.04	0–33	–	21–100
	b-TD13-CS-4	0.18 ± 0.01	0–29	–	21–100
2-CCS	a-Marble-1	$= \sigma_1$	5.0–40.0	–	21–100
	b-TD13-CS-4	$= \sigma_1$	5.0–40.0	–	21–100
3-CCS	a-Marble-1	16.9 ± 0.1	16.9–42.0	–	21–100
	b-TD13-CS-4	16.9 ± 0.1	16.9–42.0	–	21–100
	c-Marble-frac	16.9 ± 0.1	16.9–42.0	7.0–16.9 [brine] 8.0–15.5 [CO_2]	40–80 [brine] 40 [CO_2]
4-CCS[c]	a-Marble-frac	16.9 ± 0.1	16.9–40.0	7.0 ± 0.1 [brine]	21 [brine]
	b-Marble-frac	16.9 ± 0.1	16.9 ± 0.1	2.0–16.0 [brine]	21 [brine]

[a] Temperatures were increased in steps of 20 °C: 21 ± 1, 40 ± 1, 60 ± 1, 80 ± 1, and 100 ± 1 °C. In test series 3-CCS-c, the same increment of 20 °C was used till 80 ± 1 °C for brine as a pore fluid. For the CO_2-related test within series 3-CCS-c the temperature was fixed at 40 ± 1 °C. For series 4-CCS, the temperature was kept constant at 21 ± 1 °C.

[b] All experimental series, except 3-CCS-c and 4-CCS, were conducted under dry pore space conditions. In series 3-CCS-c and 4-CCS, either a 0.41 wt% NaCl-based brine solution or supercritical CO_2 was used as a pore fluid. In all tests where P_p was varied, it was increased in steps of 2.0 MPa at 0.019 MPa/s.

[c] In experimental series 4-CCS, the effect of P_p (4-CCS-b) and σ_1 (4-CCS-a) on the brine-saturated fracture permeability was investigated, next to studying the seismic response.

mm diameter) were drilled from both sides of the core sample towards the fracture (Fig. 2). In order to reach different P_p magnitudes, another ISCO pump was installed at the outlet (Fig. 2), functioning as a back-pressure, allowing for fluid flow through the fractured marble at varying levels of P_p. For the last two tests (experimental series 4-CCS in Table 2 – will be introduced in Section 2.4), where the effect of P_p and σ_1 on the (brine-saturated) fracture permeability, and on the resulting seismic velocities, was investigated, a differential pressure transducer was installed along the core length. During the experiments, active-source acoustic transmission measurements were taken for the aid of obtaining seismic velocities at the various experimental conditions studied (Table 2). We used two compressional (P-) and two shear (S-) wave transducers (SONAXIS), which had fixed positions within the two metal pistons, between which the rock sample was placed. The two sources (one P- and one S-wave) were placed in the top piston whereas the two corresponding receivers were located in the bottom piston. The active-acoustics design consists of a ring-shaped S-wave transducer (with an outer and inner diameter equal to 22 and 12 mm, respectively) and a circular P-wave transducer (10 mm diameter) located within. This design is identical for both the source- and receiver-couple. During the course of an experiment, first the P-wave source was activated and the P-wave receiver was recording. Directly afterwards the S-wave measurements were conducted in the same way. We used a WaveSurfer 422 (LeCroy) oscilloscope and a 33120A function generator (Hewlett Packard) as a waveform generator. The P- and S-wave source signals were characterised by a sine wave with a centre frequency of 200 kHz and an amplitude of 10 V. For each acoustic measurement, the signal was averaged over a total of 100 shots. One active-source acoustic transmission measurement was performed every 60 s, whereas all stresses, P_p, and strain measurements were recorded every 10 s. The complete pressure vessel, including part of the tubing/cables, was placed inside an oven, allowing for conducting the tests at elevated temperatures. Every time we altered the temperature inside the oven, we let the system equilibrate for at least 20 h. All pumps were controlled through the computer via separate Eurotherm 3504 process controllers. The experiments were performed in such a way that the following is always true: $\sigma_1 \geq \sigma_2 (= \sigma_3) \geq P_p$.

2.4. Experimental procedure: acoustic-assisted UCS and CCS

Different types of active-source acoustic-assisted tests were performed (Table 2). UCS experiments, where σ_1 increased gradually with 0.016 MPa/s and no additional $\sigma_2 (= \sigma_3)$ was imposed on the system, were conducted for both reservoir formations. For these tests, $\sigma_2 (= \sigma_3)$ was kept constant at low stresses of 0.1–0.2 MPa (Table 2) which was required for obtaining accurate measurements done by the radial extensometer. Here, the effect of increasing σ_1 on the seismic velocities was investigated for different temperatures (Table 2). Moreover, the temperature dependency of static elastic properties (i.e., Young's modulus ($E = \Delta\sigma_1/\Delta\varepsilon_a$, where ε_a represents axial strain), Poisson's ratio ($v = \Delta\varepsilon_r/\Delta\varepsilon_a$, where ε_r represents radial strain), bulk modulus ($K = E/(3 \times (1-(2 \times v)))$), and shear modulus ($G = E/(2 \times (1+v))$)) was studied as well. To avoid rock failure, σ_1 was increased to a maximum (below the yield stress) of 33 MPa and 29 MPa, for the marble (Marble-1) and calcschist (TD13-CS-4) samples, respectively. Active-source acoustic transmission measurements were taken at intervals of 5 MPa.

In addition to the UCS experiments (1-UCS series in Table 2), several CCS tests were conducted (2-CCS in Table 2), where σ_1 equalled $\sigma_2 (= \sigma_3)$ at all times during the course of a test, until a maximum of 40 MPa was reached. The associated active-source acoustic measurements were taken every 5 MPa. Between two consecutive acoustic measurements, σ_1 and $\sigma_2 (= \sigma_3)$ were increased at a rate of 0.044 MPa/s.

In experimental series 3-CCS (Table 2), $\sigma_2 (= \sigma_3)$ was kept constant at 16.9 ± 0.1 MPa whilst σ_1 increased gradually to 42 MPa with a constant rate of 0.028 MPa/s, mimicking field-representative stress conditions. Again, active-source acoustic measurements were done at intervals of 5

MPa. Varying σ_1 reflects different depths within the Kızıldere reservoir. An additional test series (3-CCS-c in Table 2) was conducted on the fractured marble (Marble-frac) sample. The artificially fractured sample allows for studying the effect of pore fluid type (Kızıldere brine versus supercritical CO_2), and P_p, on the resulting seismic velocities. Representative values for σ_1, σ_2 ($= \sigma_3$), P_p, were taken from literature (Çiftçi, 2013). Comparing series 1-UCS with 2-CCS and 3-CCS gives insights on the role of σ_2 ($= \sigma_3$) on the resulting seismic velocities.

For the last two tests (4-CCS in Table 2), a differential pressure transducer was installed over the core length for accurately monitoring the pressure drop, during flow of Kızıldere-type brine through the fracture, for the aid of fracture permeability ($k_{fracture}$) calculations. Injections rates were varied and subsequently Darcy's law (Darcy, 1856) was used for obtaining the absolute $k_{fracture}$ for the Kızıldere brine. Both the effect of σ_1 and P_p on $k_{fracture}$ and on the seismic response, were investigated. This series of measurements was performed on the Marble-frac sample at a constant temperature of $21 \pm 1 \,^\circ C$. Similar to the other experiments, active-source acoustic measurements were taken at an increment of 2 MPa in P_p (4-CCS-b), or 5 MPa in σ_1 (4-CCS-a).

In series 1-UCS, 2-CCS, and 3-CCS, the combined effect of temperature and stress on the seismic velocities was investigated. First, all experiments, i.e., UCS and CCS series, were performed at room temperature ($21 \pm 1 \,^\circ C$). Afterwards, the temperature was increased to $40 \pm 1 \,^\circ C$ and the same experiments were repeated. This procedure was repeated for $60 \pm 1 \,^\circ C$, $80 \pm 1 \,^\circ C$, and $100 \pm 1 \,^\circ C$ (except for 3-CCS-c, Table 2, for which the temperature was varied between $40 \pm 1 \,^\circ C$ and $80 \pm 1 \,^\circ C$, for brine as a pore fluid, or kept constant at $40 \pm 1 \,^\circ C$, for supercritical CO_2 as a pore fluid).

In some experiments a pore fluid was added to the system to assess its impact on the acoustic transmission measurements and $k_{fracture}$. The fluid used was either a 0.41 wt percent (wt%) sodium-chloride (NaCl)-based brine solution (density of 1001.2 kg/m^3 at atmospheric pressure and 21 $^\circ C$), with a total ionic strength equal to the original Kızıldere reservoir brine composition, or supercritical CO_2 (densities at 40 $^\circ C$ range from 277.9 to 786.3 kg/m^3 for P_p of 8 and 15.5 MPa, respectively). Table 3 gives an overview of the dynamic viscosities of the NaCl-based brine solution at varying P_p, used for $k_{fracture}$ calculations.

3. Results and discussion

3.1. UCS experiments: effect of σ_1 and temperature on seismic and static elastic properties

Multiple active-source acoustic-assisted UCS experiments were conducted on marble and calcschist samples representing reservoir formations at Kızıldere (experimental series 1-UCS in Table 2). For each sample, a total of five UCS tests were performed where the temperature was the only variable (ranging from 21 ± 1 to $100 \pm 1 \,^\circ C$). Besides investigating the impact of increasing σ_1 and temperature on the resulting seismic velocities, attention was paid to the temperature dependency of static elastic properties, which were calculated from the recorded σ_1 and axial (ε_a) and radial (ε_r) strain data.

Figs. 3 and 4 present the obtained σ_1-ε_a data for all UCS experiments done, and an overview of the static elastic parameters obtained from those experiments, respectively. The results related to the Marble-1 show a bigger range in σ_1-ε_a data, as a function of temperature, compared to the outcome for calcschist sample TD13-CS-4. This is most likely due to settling of the machine as the set-up was opened in between consecutive UCS experiments. Instead of focusing on the absolute σ_1-ε_a

levels, we rather look at the σ_1-ε_a slopes in the elastic, i.e., linear, regime, which represents the Young's modulus (E). In general, E reduces as a function of increasing temperature for both samples (Marble-1 and TD13-CS-4) studied, which is in good agreement with existing literature (Araújo et al., 1997; Dwivedi et al., 2008; Brotóns et al., 2013; Heap et al., 2013; Török and Török, 2015; Tang et al., 2019; Vagnon et al., 2019). The reason for this behaviour is most likely related to thermal hardening (i.e., thermal expansion of mineral grains). Janssen et al. (2021) shortly discussed the relatively high thermal expansion coefficients related to calcite and dolomite minerals, which are the main constituents of the marble and calcschist studied. When mineral grains tend to expand, the material's stiffness reduces, resulting in a decreasing E (Pavese et al., 1996; Liu et al., 2020). At $21 \pm 1 \,^\circ C$, the largest values for E were found: 44.6 ± 3.3 and 27.2 ± 0.4 GPa for the marble and calcschist, respectively. They gradually reduced to 35.0 ± 0.9 GPa (Marble-1) and 23.7 ± 1.1 GPa (TD13-CS-4) at $100 \pm 1 \,^\circ C$. Similar to the observations made regarding the static E, the static Poisson's ratio (ν), for Marble-1, also reduces slightly with increasing temperature between 21 ± 1 and $100 \pm 1 \,^\circ C$ (Fig. 4). This is in line with the published work of Heap et al. (2013) who assessed the temperature dependence of static and dynamic elastic properties of limestone samples from Italy and Tunisia.

Next to investigating the elastic properties of the two different rock types as a function of temperature, active-source acoustic transmission measurements were performed over the course of each UCS experiment. These measurements subsequently led to the computation of the P- and S-wave velocities, i.e., V_p and V_s, respectively. Fig. 5 presents V_p as a function of σ_1, thus burial depth in the reservoir, for both the Marble-1 (5-A) and calcschist TD13-CS-4 (5-B) core samples. Furthermore, in Fig. 5-C and D V_p is also plotted against temperature for fixed σ_1 values of 5, 10, and 25 MPa, and V_p/V_s ratios are shown as well (Fig. 5-E). For both formations, at all temperatures, V_p increases as a function of increasing σ_1, where the largest increment in V_p occurs at the lowest absolute values for σ_1. This is in agreement with earlier observations of Janssen et al. (2021) and reflects closure of potential micro-cracks, yielding increased mineral-to-mineral contact areas, thus increased V_p. This mainly occurs at σ_1<15 MPa. At higher stress levels, the amount of additional compaction that potentially can take place reduces, yielding more gradually increasing V_p trends (Pellet and Fabre, 2007; Bonnelye et al., 2017; Barnhoorn et al., 2018). From a σ_1 of roughly 15 MPa, all velocity profiles show a linear trend which can be approximated by the following two empirical relations:

$$For\ Marble.1 \rightarrow V_{p_{\sigma_1 > 15\ MPa}} = ((\sigma_1 - 15) \times 5.95) + V_{p_{\sigma_1 = 15\ MPa}} \quad (1)$$

$$For\ TD13.CS.4 \rightarrow V_{p_{\sigma_1 > 15\ MPa}} = ((\sigma_1 - 15) \times 8.12) + V_{p_{\sigma_1 = 15\ MPa}} \quad (2)$$

where $V_{p\ \sigma_1=15\ MPa}$, σ_1, and $V_{p\ \sigma_1>15\ MPa}$ represent V_P at a σ_1 of 15 MPa, the σ_1 at which one wants to obtain V_p, and the resulting V_p for the corresponding σ_1 (where σ_1>15 MPa), respectively. The above suggests that if one knows V_p at σ_1 of 15 MPa, Eqs. (1) and (2) might be used to estimate appropriate velocities for the deeper subsurface. The two empirical trends are represented by the black-dashed lines in Fig. 5-A and B.

Besides the effect of σ_1 on the seismic velocities, Fig. 5-C and D also indicates the impact of increasing temperature (from 21 ± 1 to $100 \pm 1 \,^\circ C$) on the seismic velocities. For both formations, in the entire range of σ_1 investigated, an increase in temperature yields a decrease in V_p. This behaviour was expected and has been reported by other researchers

Table 3

Dynamic viscosities of the NaCl-based brine solution at varying P_p at 21 $^\circ C$. Viscosities of the 0.41wt% NaCl-based brine were calculated using existing literature (Kestin et al., 1981; El-Dessouky and Ettouney, 2002). Values shown were used for $k_{fracture}$ calculations.

P_p (MPa)	2	4	6	7	8	10	12	14	16
Dynamic brine viscosity (mPa.s)	0.984	0.983	0.983	0.982	0.982	0.981	0.980	0.979	0.979

Fig. 5. V_p as a function of σ_1, and thus depth below surface, for the marble (A) and calcschist (B) samples investigated in experimental series 1-UCS. Vp is also plotted against temperature for values for σ_1 of 5, 10, and 25 MPa for the marble (C) and calcschist (D). Vp/Vs ratios for the marble and calcschist samples, at fixed value for σ_1 of 10 and 25 MPa, are shown in (E). The σ_1-depth trend of 23.4 MPa/km was taken from Çiftçi (2013). Note that, due to failure of the acoustics set-up, no velocity data is present at $\sigma_1 <25$ MPa for the 100 ± 1 °C test performed on the marble sample. The black-dashed lines in (A) and (B) represent Eqs. (1) and (2), respectively. The triangular data points in (A) and (B) represent acoustic measurements done during unloading of the sample (for a potential hysteresis check).

imply that the σ_1-dependency of V_p increases with increasing temperature (e.g., at 100 ± 1 °C the increase in V_p with increasing σ_1 is larger compared to 21 ± 1 °C, for both formations).

The V_p/V_s ratios in Fig. 6-E show, like before, that it seems to be independent of σ_1 (either 10 or 25 MPa). For calcschist TD13-CS-4, V_p/V_s (averaged over both σ_1 values) gradually increased from 1.69 ± 0.01 (21 ± 1 °C) to 1.80 ± 0.01 (100 ± 1 °C), which is mainly due to the relatively large reduction in V_s, with increasing temperatures, compared to V_p. The same seems to hold for the Marble-1 sample, reaching a V_p/V_s of 1.82 ± 0.01 at 100 ± 1 °C, an increase of 0.05 compared to 21 ± 1 °C.

The active-source acoustic transmission measurements done during the unloading cycles, for the hysteresis check, for the marble (Fig. 6-A), indicate roughly the same velocities as the loading-related velocities. For the calcschist (Fig. 6-B), maximum V_p differences of 1.1% (at 21 ± 1 °C and σ_1 of 20 MPa) and 1.0% (at 40 ± 1 °C and σ_1 of 20 MPa) were observed. In line with the conclusions made in the previous section (1-UCS experiments), the tests performed in 2-CCS most probably did not result in any permanent deformation to the porous media.

3.3. CCS experiments at field-representative stress conditions: effect of temperature and pore fluid on seismic properties

Next to studying the stress and temperature dependency on the seismic properties at unconfined (1-UCS) and uniform (2-CCS) stress conditions, this section presents the results related to tests performed at field-representative stress conditions (3-CCS in Table 2). Appropriate magnitudes for σ_1 and σ_2 ($= \sigma_3$), that prevail in the Kızıldere reservoir, were obtained from Çiftçi (2013) and are shown in Table 2. Besides conducting the active-source acoustic-assisted CCS tests on the dry marble (Marble-1) and calcschist (TD13-CS-4) samples, an additional series (3-CCS-c in Table 2) was carried out on an artificially fractured

marble sample (Marble-frac), where its fracture was either 100% saturated with Kızıldere-type brine or supercritical CO_2. Fig. 7 shows V_p as a function of σ_1, at a fixed σ_2 ($= \sigma_3$) of 16.9 ± 0.1 MPa, for both the dry Marble-1 (7-A) and calcschist TD13-CS-4 (7-B) core samples. V_p is also shown as a function of temperature for fixed magnitudes of σ_1 of 17.0, 25.5, and 41.7 MPa (Fig. 7-C and D). V_p/V_s ratios are shown as a function of temperature for fixed σ_1 of 17.0 and 41.7 MPa (Fig. 7-E).

Once again increasing V_p values, as function of increasing σ_1, are observed. However, the acoustic results show less variation in V_p, as function of σ_1, in comparison to the results related to series 1-UCS (Fig. 5) and series 2-CCS (Fig. 6). Main reason for this is related to the initial conditions corresponding to the first measurement. In series 3-CCS (Fig. 7) this corresponds to $\sigma_1 = \sigma_2$ ($= \sigma_3$) $= 16.9 \pm 0.1$ MPa. The elevated initial stress level entails that potential closure of microcracks, which yields increasing V_p, already occurred prior to performing the first active-source acoustic transmission measurement. The velocities shown in Fig. 7-A and B correspond well with the velocities seen in Fig. 6-A and B (i.e., uniform stress conditions). The latter implies that σ_2 ($= \sigma_3$) most likely has a negligible impact on V_p as long as σ_2 ($= \sigma_3$) is greater than, or equal to, 16.9 ± 0.1 MPa. Maximum differences in V_p obtained in series 2-CCS versus 3-CCS equal 1.7% (Marble-1) and 1.4% (calcschist TD13-CS-4). The loading process seems to take place within the elastic regime as no evidence of permanent deformation was observed (note the triangular data points in Fig. 7-A and B roughly overlapping the loading-related trend).

In terms of temperature dependency (Fig. 7-C and D), similar observations can be made as before (Figs. 5 and 6): decreasing V_p as a function of increasing temperature and its impact being larger on V_p-marble compared to V_p-calcschist. For a σ_1 of 25.5 MPa, within the temperature range of 21–80 °C, V_p decreased with 6.8% and 2.6% for Marble-1 and calcschist TD13-CS-4, respectively. Comparing these
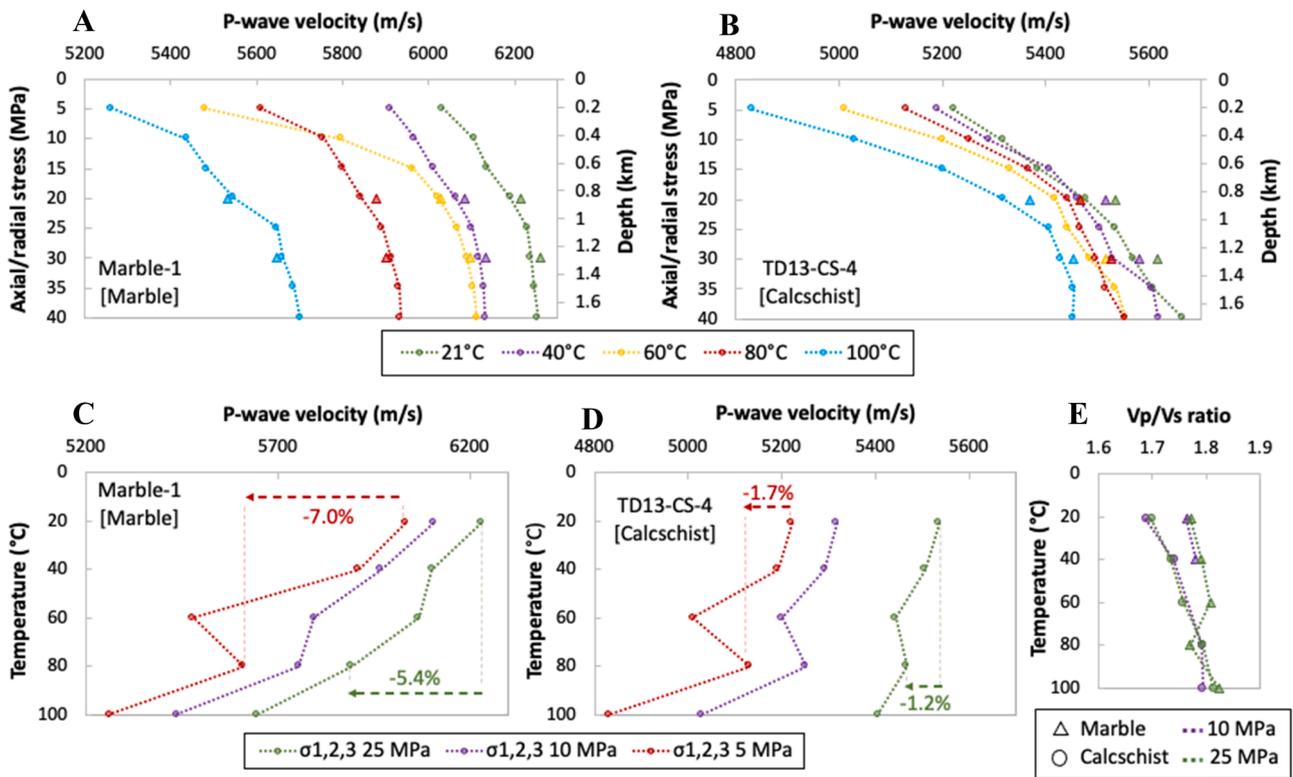
Fig. 6. V_p as a function of σ_1, and thus depth below surface, for the marble (A) and calcschist (B) samples investigated in series 2-CCS. V_p is also plotted against temperature for values for σ_1 of 5, 10, and 25 MPa for the marble (C) and calcschist (D). V_p/V_s ratios for the marble and calcschist samples, at fixed value for σ_1 of 10 and 25 MPa, are shown in (E). The σ_1-depth trend of 23.4 MPa/km was taken from Çiftçi (2013). The triangular data points in (A) and (B) represent acoustic measurements done during unloading of the sample (for a potential hysteresis check).
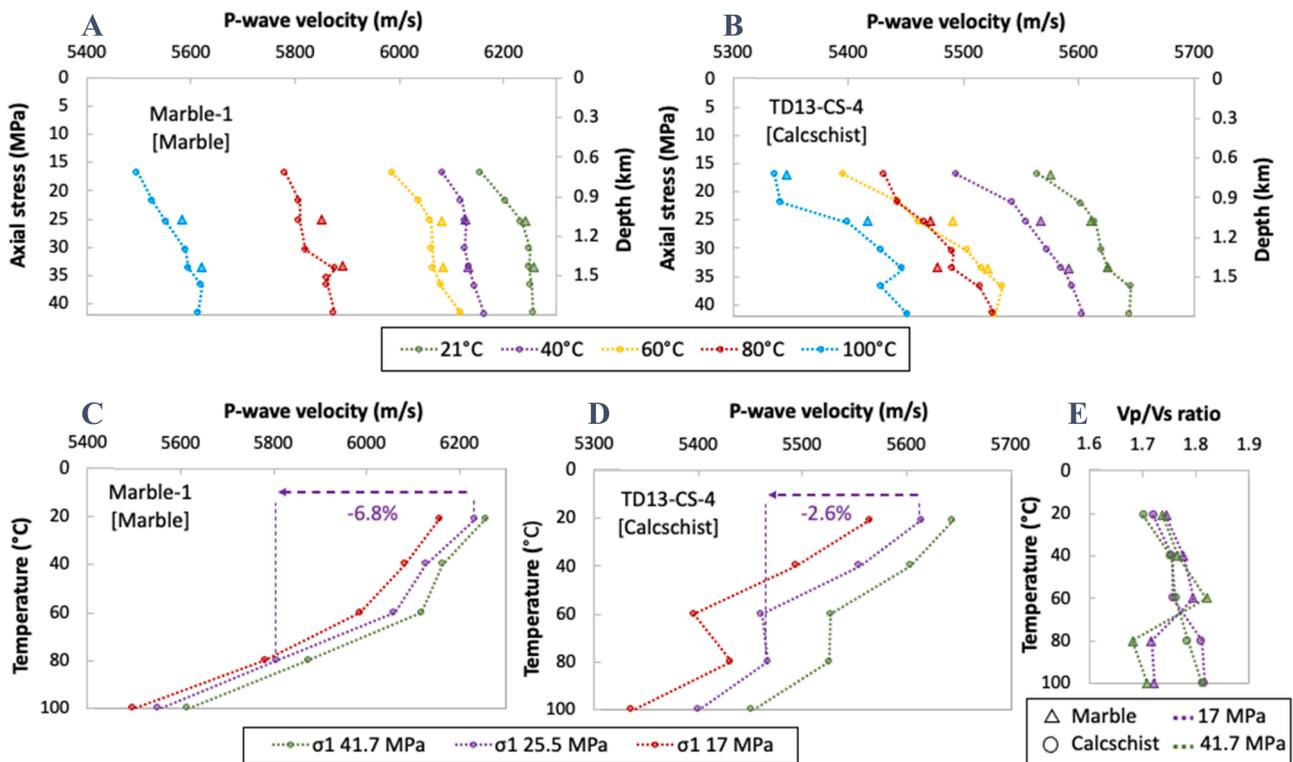
Fig. 7. V_p as a function of σ_1, and thus depth below surface, for the marble (A) and calcschist (B) samples investigated in series 3-CCS. V_p is also plotted against temperature for values for σ_1 of 17.0, 25.5, and 41.7 MPa for the marble (C) and calcschist (D). V_p/V_s ratios for the marble and calcschist samples, at fixed value for σ_1 of 17.0 and 41.7 MPa, are shown in (E). The σ_1-depth trend of 23.4 MPa/km was taken from Çiftçi (2013). The triangular data points in (A) and (B) represent acoustic measurements done during unloading of the sample (for a potential hysteresis check).

values to the decrease in V_p, within the same temperature range, at uniform stress conditions of $\sigma_1 = \sigma_2 = \sigma_3 = 25$ MPa (5.4% and 1.2% for Marble-1 and calcschist TD13-CS-4, respectively), we may conclude that the temperature effect is of a lower magnitude when imposing uniform stress conditions on a sample, reducing the potential for minerals to expand with increasing temperature.

Similar to the observations made in the previous sections, σ_1 (17.0 or 41.7 MPa) seems to have a negligible effect on the resulting V_p/V_s ratios (Fig. 7-E). The averaged V_p/V_s ratio, as a function of temperature, corresponding to calcschist TD13-CS-4 sample shows similar behaviour to the uniform stress conditions (2-CCS): gradual increase from 1.71 ± 0.01 (21 ± 1 °C) to 1.81 ± 0.01 (100 ± 1 °C). For Marble-1, no distinctive trend could be identified.

Besides investigating the combined temperature and stress effect on the seismic properties, the effect of pore fluid (Kızıldere-type brine, i.e., 0.41 wt% NaCl-based brine, versus supercritical CO_2) and P_p were also assessed. The latter was done using an artificially fractured marble sample: Marble-frac (Section 2.4). Fig. 8 presents V_s, V_p, and the V_p/V_s ratios as a function of increasing σ_1 and P_p, at a fixed σ_2 ($=\sigma_3$) of 16.9 ± 0.1 MPa, for Marble-frac (Table 1). Note that the results shown in Fig. 8 reflect a 100% brine-saturated fracture.

Increasing V_p values, as a function of increasing σ_1 and P_p, are observed. In terms of absolute velocities, V_p of Marble-frac, fully saturated with brine, is higher than the V_p values shown in Fig. 7-A (i.e., the velocities related to a dry, intact, marble – Marble-1). The trend related to V_s differs from the observations made regarding V_p. Here, V_s shows a slight decrease as a function of increasing σ_1 and P_p. The latter is fully related to the individual effects of σ_1 and P_p on V_s: the negative impact of an increasing P_p has a larger effect on V_s compared to the positive impact of an increasing σ_1 (will be discussed in detail in Section 3.4). The V_p/V_s ratios presented show a slightly increasing ratio as a function of increasing σ_1 and P_p, which can be explained by the aforementioned behaviour of V_s and V_p. Moreover, the V_p/V_s ratios exhibit higher values when compared with the experiment conducted on the dry, intact, Marble-1 (Fig. 7-E). This is mainly a consequence of the decrease in V_s (of roughly 12%) due to the presence of the fluid-filled artificial fracture.

At a temperature of 80 ± 1 °C, between σ_1 of 18 and 40 MPa, V_p increased with roughly 1.8%. For the same range in σ_1, at a temperature of 40 ± 1 °C, V_p increased only with approximately 0.6%. This suggests, as discussed before, that at higher temperatures, minerals have more tendency to expand, which gives rise to more potential space available for compaction, thus for increasing V_p.

Subsequent to performing experiments on a fully brine-saturated Marble-frac, one separate experimental series was performed – utilizing the same Marble-frac sample but with a 100% supercritical CO_2-saturated fracture. These experiments were conducted at 40 ± 1 °C (Table 2).

So far, we mainly focused on first arrivals, i.e., V_p and V_s. However, in order to differentiate between a supercritical CO_2-filled fracture versus a fully brine-saturated crack, first-arrival analyses might not be sensitive enough as they are very similar for both the P- (Fig. 9-A) and S-wave (Fig. 9-B). Fig. 9-A shows the recorded signal (P-wave) for both the brine- and CO_2-case at a temperature of 40 ± 1 °C for varying σ_1 and P_p while σ_2 ($=\sigma_3$) was constant at 16.9 ± 0.1 MPa. As mentioned before, the first-arrival time, and thus V_p, is almost identical in both cases. The aperture of the man-made fracture, in the order of tens of microns, is significantly smaller than the wavelengths (wavelengths at $\sigma_1 = 32$ MPa, and for the centre frequency of 200 kHz, in Fig. 9 equalled 31.0 and 14.5 mm for the P- and S-wave, respectively). The latter implies that the tuning thicknesses, i.e., one-quarter of the wavelengths and equal to 7.8 mm (P-wave) and 3.6 mm (S-wave), is too large to observe any effect in transmission arrival times (Robertson and Nogami, 1984; Janssen, 2018; Chadwick et al., 2019). Although the first-arrival times are hardly different, we can clearly discern differences in the amplitude of the two arrivals, which suggests that the thin brine- or CO_2-saturated fracture did affect the overall elastic properties across that interface (Hudson and Liu, 1999; Mavko et al., 2020). It is obvious that when the fracture is completely filled with supercritical CO_2, the recorded peaks and troughs of the P-wave arrival are of lower absolute value compared to the fully brine-saturated case (Fig. 9-A). A possible explanation could be that, when filled with supercritical CO_2, the contrast in the acoustic impedance (between the matrix and the fracture) is higher, due to its lower fluid density, compared to the brine-saturated situation (Table 4 gives an overview of fluid densities at varying P_p, where the fluid density difference reduces with increasing P_p). This implies that, in the CO_2-saturated case, more P-wave energy is reflected, hence less energy is left for transmittance, which results in lower peak and trough amplitudes being measured. Besides a potential change in the top-fracture reflection coefficient, it is expected that the P-wave intrinsic attenuation is higher for the supercritical CO_2-saturated case versus a fully brine-saturated fracture, suggesting more loss of wave energy for propagation through a CO_2-filled fracture (Ekanem et al., 2016).

Fig. 9-B presents the recorded S-wave arrival, for the brine- and CO_2-saturated cases, at the same stress and temperature conditions as for the P-wave measurements in Fig. 9-A. In general, the same observations can be made for the recorded transmitted S-wave: slightly lower peak and trough amplitudes for the CO_2-saturated case. The fact that we are able to record the S-wave implies that either the mechanical aperture (i.e., opening of the fracture) is zero at some locations in space (allowing for the S-wave to propagate within the matrix), and/or the S-wave
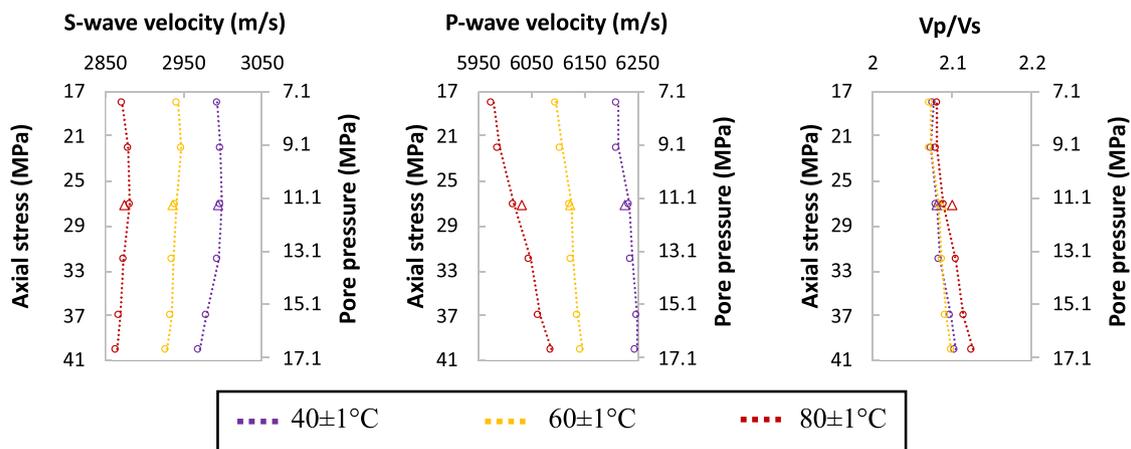
Fig. 8. V_s (left), V_p (centre), and the V_p/V_s ratios (right) as a function of σ_1 and P_p, and thus depth below surface, for the artificially fractured marble (Marble-frac in Table 1) studied in series 3-CCS-c. Note that the results shown reflect a 100% brine-saturated fracture. Field-representative values for σ_1 and P_p were taken from Çiftçi (2013). The triangular data points represent acoustic measurements done during unloading of the sample (for a potential hysteresis check).
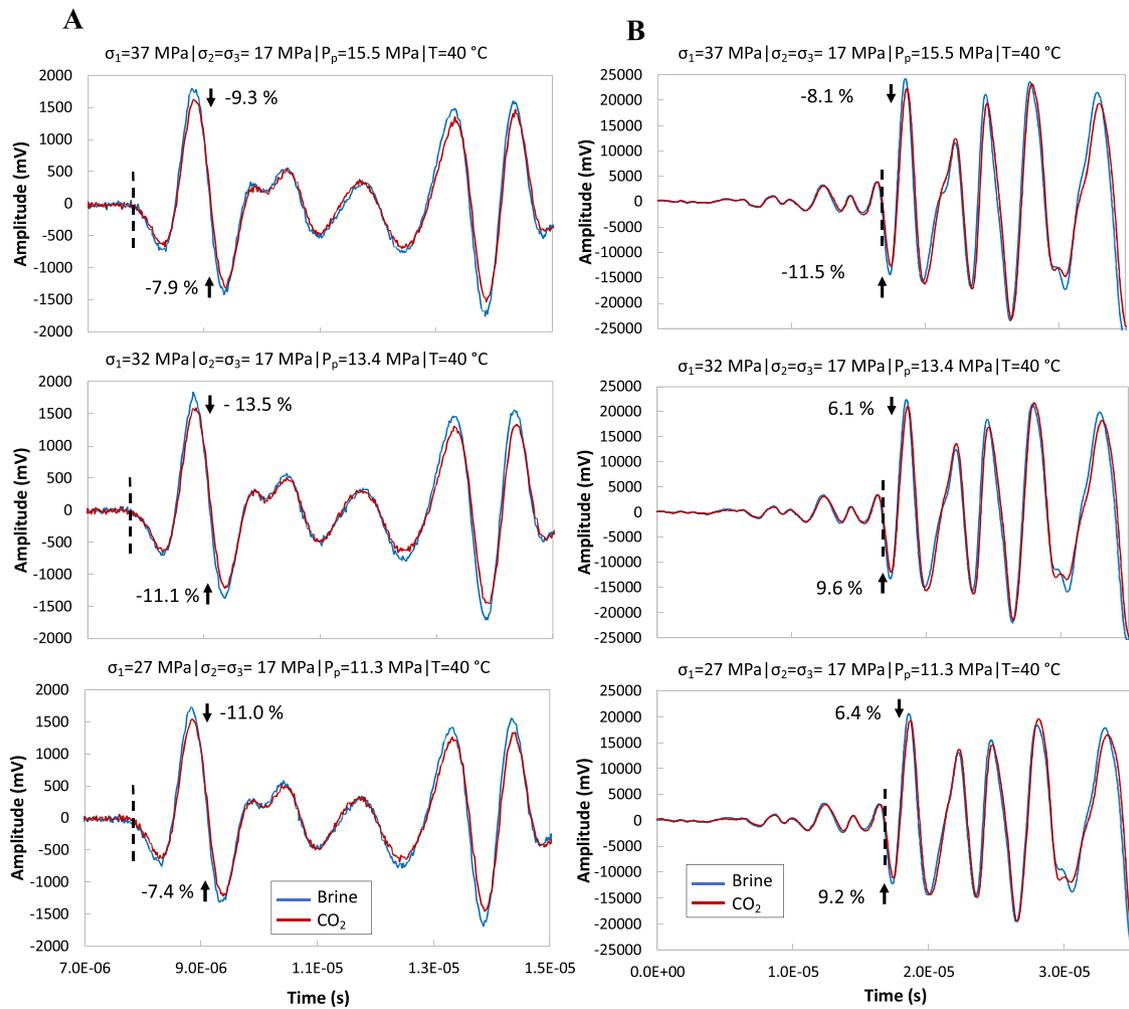
Fig. 9. Recorded P-wave (A) and S-wave (B) signals in active-source transmission measurements for the brine-saturated fracture (blue) and the fully supercritical CO_2-saturated fracture (red). Both σ_1 and P_p were varied according to field-representative conditions taken from Çiftçi (2013). One temperature was assessed: $40 \pm 1 \,^{\circ}C$. The black-dashed lines indicate the picked onset of the time of the first P- and S-wave arrivals, which are quite identical for both situations investigated. For the first and second peak or trough, the decrease in amplitude (in %), between brine- and CO_2-saturated fracture for both the P- and S-wave, is shown.

Table 4
Fluid densities for 0.41 wt% NaCl-based brine (Potter and Brown, 1977; El-D-essouky and Ettouny, 2002) and supercritical CO_2 (Goos et al., 2011) at a P_p of 8.0 and 15.5 MPa and a temperature of 40 °C.

P_p (MPa)	8.0	15.5
Density brine (kg/m^3)	998.0	1001.4
Density CO_2 (kg/m^3)	277.9	786.3

wavelength (14.5 mm at $\sigma_1 = 32$ MPa in Fig. 9) is much longer than the fracture aperture (tens of microns), so that the S-wave may propagate 'over' the fracture interfaces. For the former case, the coupling between top and bottom marble differs as a function of pore fluid. For the supercritical CO_2-case, the coupling might be less (e.g., as a result of calcite/dolomite dissolution processes of which the rate depends on CO_2 concentrations (Pokrovsky et al., 2009; Ghosh and Sen, 2012)), directly implying a longer matrix-travel path for the S-wave, thus more attenuation, hence less energy recorded. For the latter case, our observations are fully related to the type of pore fluid, suggesting that the overall shear modulus is affected by pore fluid type (Mavko and Jizka, 1991; Berryman, 2005).

3.4. CCS experiments: effect of P_p and σ_1 on the brine-saturated fracture permeability and seismic properties

Besides investigating the temperature and stress dependency of the seismic characteristics at unconfined (1-UCS), uniform (2-CCS), and field-representative (3-CCS) stress conditions, here we present experimental results related to series 4-CCS (Table 2) with which the effect of P_p and σ_1 on the (brine-saturated) fracture permeability, and seismic velocities, were assessed. The same artificially fractured marble (Marble-frac in Tables 1 and 2) was used for this purpose. In experiment 4-CCS-a, $\sigma_2 (= \sigma_3)$ was kept fixed at 16.9 ± 0.1 MPa and P_p was set at 7.0 ± 0.1 MPa, whilst σ_1 increased gradually from 16.9 ± 0.1 to 40.0 ± 0.1 MPa. In 4-CCS-b, all stresses, i.e., σ_1 and $\sigma_2 (= \sigma_3)$, were kept constant at 16.9 ± 0.1 MPa, whereas the P_p was varied from 2.0 ± 0.1 to 16.0 ± 0.1 MPa. The experiments were conducted at a constant temperature of $21 \pm 1 \,^{\circ}C$.

Fig. 10 presents V_p (A), V_s (B), and the V_p/V_s ratio (C) as a function of increasing σ_1, thus depth, for experiment 4-CCS-a. Moreover, the absolute $k_{fracture}$ to 0.41 wt% NaCl brine is also shown as a function of increasing σ_1 (D) and as a function of V_p (E). Similar to the results above, increasing seismic velocities were observed as a function of increasing σ_1. Both V_p and V_s increased rather rapidly till σ_1 equalled 27 MPa, after which the velocities increased in a more gradual way. This implies that most axial elastic deformation occurs at lower stress levels. For a σ_1 from
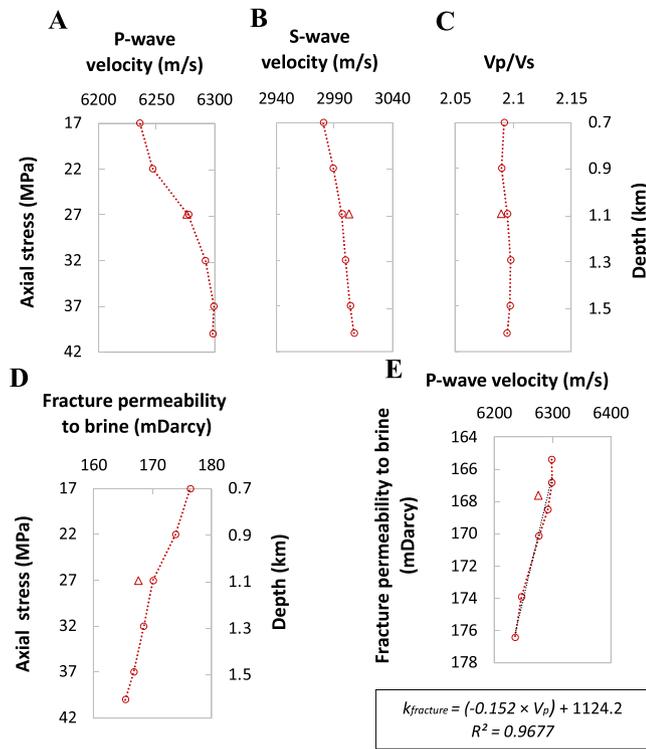
Fig. 10. Experimental results for series 4-CCS-a (Table 2): (A) V_p, (B) V_s, (C) V_p/V_s, and (D) $k_{fracture}$ as a function of increasing σ_1 and thus depth. The σ_1-depth trend of 23.4 MPa/km was taken from Çiftçi (2013). Moreover, $k_{fracture}$ is also plotted as a function of (E) V_p. The good fit of the linear regression indicates that one can estimate $k_{fracture}$ based on the V_p profile obtained. The triangular data points represent measurements done during unloading of the sample (for a potential hysteresis check).

Fig. 11. Experimental results for series 4-CCS-b (Table 2): (A) V_p, (B) V_s, (C) V_p/V_s, and (D) $k_{fracture}$ as a function of increasing P_p and thus depth. The P_p-depth trend of 9.8 MPa/km was taken from Çiftçi (2013). Moreover, $k_{fracture}$ is also plotted as function of (E) V_p. The good fit of the linear regression indicates that one can estimate $k_{fracture}$ based on the V_p profile obtained. The triangular data points represent acoustic measurements done during unloading of the sample (for a potential hysteresis check).

17 to 37 MPa, V_p and V_s increased with 1.0 and 0.8%, respectively. The increases in velocity are slightly lower compared to values for the dry, intact, Marble-1 sample studied in experiment 3-CCS-a (same stress conditions at 21 ± 1 °C): 1.6% (V_p) and 1.4% (V_s). The V_p/V_s ratio stays relatively constant – averaged V_p/V_s ratio of 2.09 ± 0.01 over the entire stress range studied (compared to 1.75 ± 0.01 for the dry intact Marble-1 in series 3-CCS-a at 21 ± 1 °C). The V_p/V_s ratios for the dry and fracture-saturated marbles correspond well with the results in Wang et al. (2012), who investigated V_p/V_s ratios for wet and dry Carrara marbles. Beside velocity-related data, Fig. 10-D shows $k_{fracture}$ to Kızıl-dere brine as a function of σ_1. The fracture permeability reduces as a function of increasing σ_1 from 176.4 ± 3.0 mDarcy (at $\sigma_1 = 16.9 \pm 0.1$ MPa) to 165.4 ± 2.6 mDarcy (at $\sigma_1 = 40.0 \pm 0.1$ MPa), a reduction of 6.2%. The parameter $k_{fracture}$ is mainly controlled by the mechanical aperture and the fracture roughness (Brown, 1987; Muralidharan et al., 2004; Lavrov, 2017). The decreasing $k_{fracture}$ (Fig. 10-D) is likely due to closure of the mechanical aperture of the fracture when σ_1 increases and $\sigma_2 (= \sigma_3)$ and P_p stay constant. It is expected that the fracture roughness is less affected by the varying σ_1. Whereas the seismic velocities increased relatively rapidly till $\sigma_1 = 27$ MPa, $k_{fracture}$ decreased promptly within the same stress range, suggesting that most of the aperture closure occurred at $\sigma_1 \leq 27$ MPa, yielding a relatively sharp decrease in $k_{fracture}$. To focus in more detail on the relationship between V_p and $k_{fracture}$, both parameters were plotted against each other (Fig. 10-E). The plot clearly shows an inversely proportional relationship where $k_{fracture}$ increases with decreasing V_p. The linear regression shows a goodness-of-fit (i.e., R^2) of 0.9677, indicating a strong fit between the model and the data.

Fig. 11 shows V_p (A), V_s (B), V_p/V_s ratio (C), and $k_{fracture}$ as a function of increasing P_p, thus depth (D), for experiment 4-CCS-b. Additionally, similar as above, $k_{fracture}$ is also shown as a function of V_p (E). Both V_p and
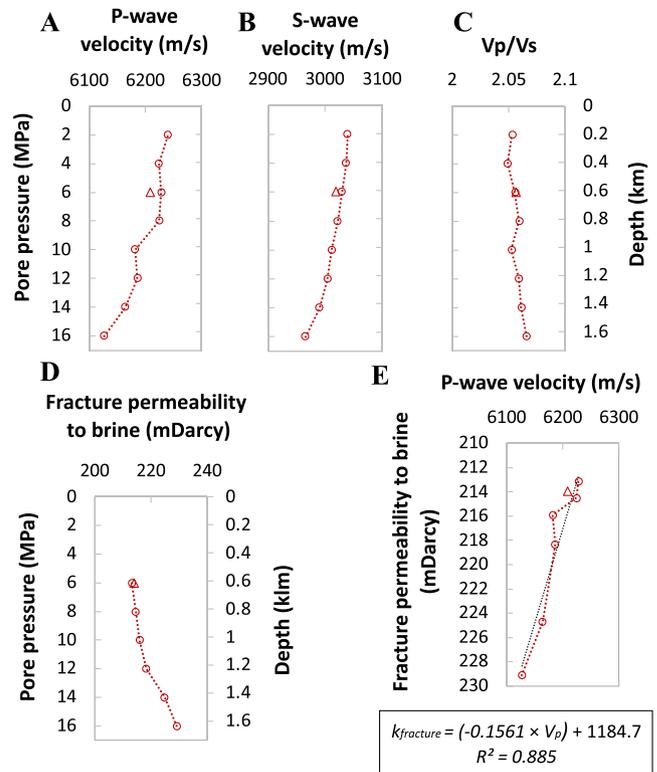
V_s decrease with increasing P_p. The main reason for this is that, as a consequence of increasing P_p, the forces that act on the contact surfaces between grains (or minerals) reduce, yielding a lower velocity. Between a P_p of 2 and 16 MPa, V_p and V_s reduced with 1.8 and 2.4%, respectively. The latter directly implies that V_s is more sensitive to changes in P_p compared to V_p, which is in agreement with published laboratory measurements (Christensen and Wang, 1985; Hornby, 1996; Xu et al., 2006) and theoretical work (Furre, 2002; Liu et al., 2002). In Fig. 8 we observed a decreasing V_s, and an increasing V_p, as a function of increasing σ_1 and P_p. This can now be explained by the fact that the positive effect of increasing σ_1 on velocities is larger for V_p and smaller for V_s (Fig. 10-A and B), whereas the negative impact of an increasing P_p is smaller for V_p and larger for V_s (Fig. 11-A and B). For V_s in Fig. 8, the increase in P_p has a larger impact on the velocity than the increasing σ_1.

The V_p/V_s ratio (Fig. 11-C) stays rather constant (2.06 ± 0.01), though a small increasing trend might be identified from a P_p of 10 MPa onward (which is fully related to the fact that V_s is more sensitive to changes in P_p). Compared to experiment 4-CCS-a (Fig. 10-C), the ratio is slightly lower at the same stress conditions (2.06 versus 2.09). This can be attributed to a slightly higher V_s in experiment 4-CCS-b with respect to 4-CCS-a, at the same conditions. This, most likely, is related to the fracture aperture not being constant for both experimental series as it experienced multiple stress levels between the two experiments, which might affect the initial aperture per experiment.

Similar to the velocity data, the impact of P_p on $k_{fracture}$ (experiment 4-CCS-b) shows the opposite effect compared to the impact of σ_1 on $k_{fracture}$ (experiment 4-CCS-a): increasing $k_{fracture}$ with increasing P_p (Fig. 11-D). Where $k_{fracture}$ increases only gently with 2.4% between a P_p of 6 and 12 MPa, for pressures above that (12–16 MPa) a sharper increase in $k_{fracture}$ is seen (4.9% increase), in line with the decreasing

trends in the velocity data. As discussed above, $k_{fracture}$ mainly depends on the mechanical aperture and the roughness of the fracture. It is expected that the observed increase in $k_{fracture}$ comes from opening of the fracture, i.e., increasing its aperture, due to an increase in P_p. Like in the previous experiment, $k_{fracture}$ was plotted as a function of V_p and a linear regression was carried out (Fig. 11-E). Again, we obtain a good linear fit between the model and data. Note that the gradient in the two experiments (0.1520 in 4-CCS-a versus 0.1561 in 4-CCS-b) are very similar. Only the intercepts (1124.2 in 4-CCS-a versus 1184.7 in 4-CCS-b) differ. The latter is a result of the fact that the absolute values for $k_{fracture}$, between 4-CCS-a and 4-CCS-b, are similar but not exactly the same. This is most probably related to the initial mechanical fracture aperture not being constant for both tests, affecting the initial absolute $k_{fracture}$ per experiment. Hence, for analyses purposes, we rather focus on the change, i.e., gradient, of $k_{fracture}$ instead of its absolute values.

4. General discussion

In this section, the results presented and observations made in this paper will be discussed in terms of the combined temperature, σ_1, and P_p effect on V_p and V_s. Moreover, potential experimental implications will be scrutinized in the broadest framework possible.

4.1. Combined temperature, σ_1, and P_p effect on V_p and V_s of the fractured marble

Multiple experimental measurements were conducted aiming at studying the individual impact of σ_1 (1-UCS, 3-CCS-a/b, and 4-CCS-a), P_p (4-CCS-b), and temperature (1-UCS, 2-CCS, and 3-CCS-a/b) on the resulting seismic velocities. Series 3-CCS-c, where the fractured marble was 100% brine-saturated, is the only experimental measurement series performed where all three parameters (temperature, σ_1, and P_p) were altered. While σ_1 and P_p were changed according to field-representative conditions, the temperature was set at 40, 60, and 80 °C, because the reservoir temperature, of up to 240 °C, could not be reached with the laboratory set-ups we used. In order to analyse the relationship between V_p and V_s and the three variables (temperature, σ_1, and P_p) all together, multiple nonlinear regression was carried out on the accumulated V_p and V_s datasets consisting of all experimental series where the 100% brine-saturated fractured marble was utilized: 3-CCS-c (brine-saturated), 4-CCS-a, and 4-CCS-b (Table 2). The multiple nonlinear regression technique led to the following two second-degree polynomial relationships:

$$V_p = 6105.62 + 10.17\sigma_1 - 7.78P_p + 1.43T - 0.09\sigma_1^2 + 0.11P_p^2 - 0.05T^2 \quad (3)$$

$$V_s = 3019.22 + 0.28\sigma_1 - 5.99P_p + 1.80T - 0.01\sigma_1^2 + 0.16P_p^2 - 0.04T^2 \quad (4)$$

where T, σ_1, and P_p represent the temperature in °C, the axial stress in MPa, and the pore pressure in MPa. Note that Eqs. (3) and (4) hold only for the experimental conditions imposed in series 3-CCS-c (brine-saturated fracture) and 4-CCS-a+b. Figs. 12 and 13 present, for series 3-CCS-c and 4-CCS-a+b, the measured versus predicted V_p and V_s, respectively.

Eqs. (3) and (4) summarize the combined effects of temperature, σ_1, and P_p, which we observed and discussed in previous sections. Following our observations, Eq. (3) clearly indicates a positive impact of an increasing σ_1 on V_p, a negative effect of increasing P_p on V_p, and a negative impact of increasing temperature on V_p. For instance, when comparing measured marble V_p values of 3-CCS-a (Fig. 7-A) with the ones of 4-CCS-a (Fig. 10-A), between a σ_1 of 17 and 37 MPa and at a temperature of 21 ± 1 °C, we see that V_p of the dry, intact, marble increased with roughly 1.6% compared to approximately 1.0% for the brine-saturated fractured marble. The lower gradient for the 100% brine-saturated fractured marble is fully related to the impact of a fixed P_p of 7.0 ± 0.1 MPa, tending to reduce the rate at which V_p increases with increasing σ_1 (Eq. (3)).

For V_s, i.e., Eq. (4), we can make similar observations. However, here the impact of an increasing σ_1 on V_s is significantly smaller compared to V_p (Eq. (3)). This, combined with a relatively large impact of P_p on V_s, results in decreasing predicted V_s values as a function of increasing σ_1 and P_p (Fig. 13-A). The latter we have observed during our experiments for values of σ_1 and P_p of 27 and 11 MPa or higher, respectively. When the three required variables are known, one might use Eqs. (3) and (4) to estimate V_p and V_s for Kızıldere marble.

4.2. Experimental implications

For all experimental measurement series (Table 2) the same intact marble (Marble-1), fractured marble (Marble-frac), and intact calcschist (TD13-CS-4) samples were used (Table 1). This was explicitly done for comparison purposes, i.e., to avoid any potential heterogeneity effect amongst different core samples. Though this methodology favours comparison between a single rock sample, a potential risk exist that the internal pore structure of the porous medium might be altered during one of the first tests conducted on an individual sample. This can lead to the sample not being representative anymore of its initial condition, finally resulting in comparison implications amongst experimental series. In order to asses this, active-source acoustic transmission measurements were conducted during unloading of the sample, i.e., after a specific experiment was performed. These measurements are represented by the triangular data points in Figs. 5–8 and 10, 11. The
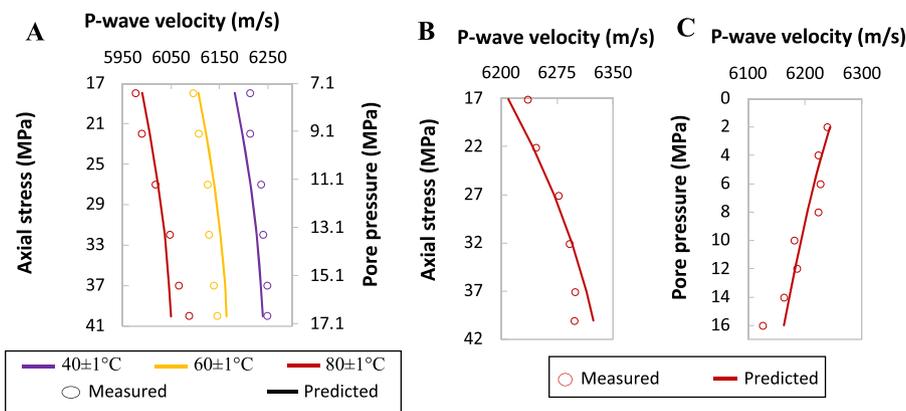
Fig. 12. Measured versus predicted V_p values in (A) experiment 3-CCS-c, (B) experiment 4-CCS-a, and (C) experiment 4-CCS-b (Table 2 and Figs. 8, 10, and 11). Maximum differences between measured and predicted V_p equals in (A) 0.62% (at 80 °C and σ_1 = 40 MPa), in (B) 0.41% (at σ_1 = 17 MPa), and in (C) 0.59% (at P_p = 16 MPa).
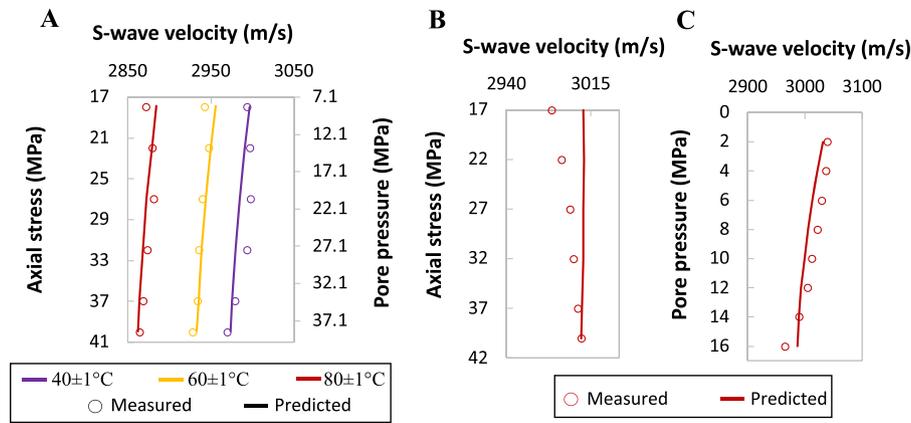
Fig. 13. Measured versus predicted V_s values in (A) experiment 3-CCS-c, (B) experiment 4-CCS-a, and (C) experiment 4-CCS-b (Table 2 and Figs. 8, 10, and 11). Maximum differences between measured and predicted V_s equals in (A) 0.48% (at 40 °C and σ_1 = 32 MPa), in (B) 0.95% (at σ_1 = 17 MPa), and in (C) 0.71% (at P_p = 16 MPa).

unloading measurements generally follow the loading trend quite accurately, with maximum differences in V_p in the order of 1%, suggesting that all deformation occurred in the elastic regime (i.e., no permanent alteration of the internal pore structure).

As mentioned in Section 2.4, for experimental series 3-CCS-c and 4-CCS (Table 2) a simplified NaCl-based model brine was prepared with a total ionic strength equal to the original Kızıldere reservoir brine composition. Although we kept the total concentration of ions in solution constant at 0.07 mol/L, the type of ions present differs. Whilst the model brine only includes Na^+ and Cl^-, the original Kızıldere reservoir brine composition contains mainly HCO_3^- and Na^+ ions, and smaller amounts of SO_4^{2-} and H_2CO_3. The different chemical composition might effect dissolution processes of the marble and calcschist studied. For example, the original Kızıldere reservoir brine contains H_2CO_3 (carbonic acid), which might promote dissolution of the calcite minerals.

In Section 3.3 (Fig. 9) we studied the effect of pore fluid type (brine versus supercritical CO_2), in the artificially fractured marble (series 3-CCS-c), on the acoustic transmission measurements. The results showed that the first arrivals, of both the P- and S-waves, are very similar and cannot be used for differentiating between the two fracture-filled pore fluids. This is most likely related to the small fracture aperture (in the order of tens of microns) compared to the source-signal wavelength (in the order of tens of millimetres). As the results shown in Fig. 9 are relevant for a temperature of 40 ± 1 °C only, one might wonder if the same effect would be observed at higher temperatures. For this reason, we performed more P-wave transmission measurements at a constant temperature of 80 ± 1 °C. Corresponding results indicated that the same phenomenon, as previously discussed at 40 ± 1 °C, can be observed at 80 ± 1 °C.

We discussed the effect of P_p, at fixed values for $\sigma_1 = \sigma_2 = \sigma_3$, on V_p (at a constant temperature of 21 ± 1 °C) in Section 3.4 (Fig. 11-A). We observed decreasing V_p with increasing P_p due to a reduction of the forces that act on the mineral contact surfaces (i.e., opening of the fracture). Note that these observations are valid for a 100% brine-saturated fracture at the aforementioned temperature. One may ask whether the type of pore fluid might affect the observed P_p-V_p relationship. For this purpose, we performed additional experiments where we compare a 100% brine-saturated versus supercritical CO_2-saturated fracture, at a fixed temperature of 40 ± 1 °C (Fig. 14).

From Fig. 14 we can conclude that the effect of P_p on V_p seems to be independent of pore fluid type, as the CO_2-related data points fall in line with the corresponding results for brine. In theory, pore fluid type does affect V_p, as P-waves tend to travel faster in the relatively dense brine compared to supercritical CO_2. However, as discussed above, most probably the fracture aperture is too small, compared to the P-wave
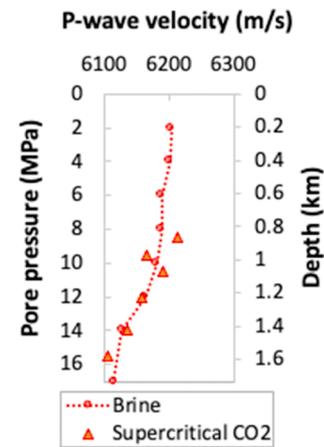
Fig. 14. Comparison of a 100% brine saturated versus 100% supercritical CO_2-saturated fracture: effect of P_p on V_p. The P_p-depth trend of 9.8 MPa/km was taken from (Çiftçi, 2013). A fixed $\sigma_1 = \sigma_2 = \sigma_3$ of 17 MPa was used. The temperature was held constant at 40 ± 1 °C, so that only P_p and pore fluid type were varied.

wavelength, i.e., an estimated wavelength-to-aperture ratio of a few hundred, to yield distinguishable differences in first-arrival times.

4.3. From the laboratory to the field

The experiments performed and described above resulted in several recommendations for the active-source monitoring acquisition at Kızıldere. They include conducting a baseline acquisition prior to the injection of CO_2 (i.e., at fully brine-saturated conditions) for comparison purposes and ensuring that each monitoring campaign is performed using the exact same acquisition parameters (i.e., the only variable is the concentration of injected CO_2). Another recommendation is to focus on the amplitude of the recorded reflections for investigating the effect of CO_2 when the aperture of the fluid-filled fracture systems (ranging from tens of microns to several mm – Fig. 1-B) are orders of magnitudes smaller than the source wavelengths (typically tens of meters in the field). In order to visualize the latter, we made a preliminary subsurface model of the Kızıldere geothermal system. Subsequently, we used the measured seismic velocities, as a function of depth, for the brine- and CO_2-saturated cases (Fig. 9) for one specific marble layer in the model. Finite-difference 2D acoustic modelling (Thorbecke and Draganov, 2011) with grid sizes of 3×3 m was conducted and the results (in the

form of single shot gathers) are shown in Fig. 15. One source location (at $x = -500$ m and $z = 0$ m) was modelled. Receivers were placed at the surface with an interval of 5 m. In the model, the top boundary, i.e., the earth's surface, was set as a free surface, while the other three boundaries were set to be absorbing. The source function was characterised by a Ricker wavelet with a frequency peak of 50 Hz. The subsurface model extends 1000 m in the lateral direction (334 grid blocks) and 2500 m in depth (834 grid blocks). As seen in Fig. 15-D, the difference gather (i.e., shot gather for a marble layer with CO_2 – shot gather for a marble layer with brine) show very clear near-offset amplitude differences at a depth of around 0.9 s two-way traveltime (TWT). This is the effect of replacing brine with supercritical CO_2 in the third marble layer in our subsurface model. It visualizes our experimental observations presented in this work: for distinguishing between a supercritical CO_2-saturated fracture and a fully brine-filled fracture, one could focus on amplitude differences.

As discussed above, reflection arrivals from the bottom of the target marble layer, but also from below the target layer, might present also time differences for the two cases. In the difference panel in Fig. 15-D, also this effect, combined with amplitude effects, can be observed, e.g., for arrivals later than 1 s. TWT. Note, that using reflections from below the target should be done with caution as possible changes of the seismic properties below the reservoir might lead to erroneous interpretation.

5. Conclusions

As part of a novel seismic monitoring project in the Kızıldere (Turkey) geothermal field, where the feasibility of re-injection and storage of produced CO_2 is being investigated, we conducted a P- and S-wave seismic velocity (V_p and V_s, respectively) characterisation study. Our study involved comprehensive laboratory measurements on the combined stress (up to 42 MPa), pore pressure (up to 17 MPa), pore fluid type (model brine or supercritical CO_2), and temperature (up to 100 ± 1 °C) dependence of seismic properties in the two main metamorphic reservoir formations that make up the second reservoir at the Kızıldere geothermal system: marble and calcschist. The performed experiments involved well-controlled acoustic-assisted (un)confined compressive strength tests, next to texture and mineralogical analyses utilizing thin sections, X-ray diffraction (XRD) and fluorescence (XRF), and micro-computed-tomography (micro-CT) techniques. Our study resulted in the following main conclusions:

- The synthetical XRF analysis revealed that the chemical composition of the Kızıldere marble consists of >97 wt% calcium oxide and >1 wt % magnesium oxide. Its mineralogy, exposed by XRD and thin section studies, confirms that it mainly includes recrystallized calcite and some dolomite. Texture analysis of thin section material showed that the presence of fractures increased the 2D marble permeability by approximately a factor 20, verifying the fracture-dominated flow.
- Each UCS experiment revealed a similar trend where at first a sharp increase in V_p was seen at relatively low axial stress levels (up to roughly 15 MPa) due to initial compaction, followed by a more moderate increase at higher stress levels. Moreover, UCS data implied that the stress-dependency of V_p increased as a function of increasing temperature, suggesting more potential space available for compaction at higher temperatures.
- All acoustic-assisted compressive strength experiments showed the same temperature- dependency of V_p where an increase in temperature resulted in a decrease in V_p. It is controlled by the thermal expansion of constituting minerals. The temperature effect on V_p increased with reducing stress, as lower stress levels allow for more potential thermal expansion.
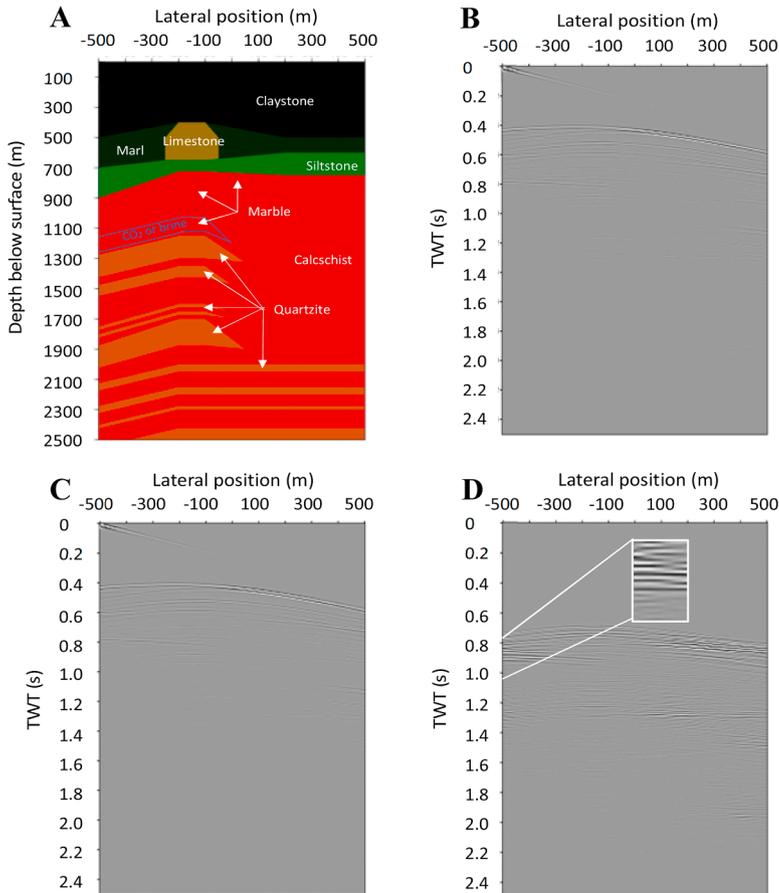
Fig. 15. (A) Kızıldere subsurface model for which the velocity model was taken from our earlier work (Janssen et al., 2021) except for the third marble layer (shown by the blue outline), for which CO_2- and brine-saturated velocities from the laboratory measurements (Fig. 9) were used. Single shot gather for the case of the marble layer saturated with (B) CO_2 and (C) brine. (D) Difference panel after subtraction of C from B. The amplitudes in the difference panel were increased with a factor 1000 for visualization purposes. Only one source location was modelled, i.e., at $x = -500$ m. Receivers were placed at the surface with a spacing of 5 m. TWT stands for two-way traveltime.

- UCS-related results revealed that Young's modulus reduced as a function of increasing temperature for both lithologies assessed. This behaviour is most probably related to thermal expansion of the mineral grains, reducing the rock's stiffness.

- Comparison between CCS experiments conducted at uniform and reservoir stress conditions suggested that the impact of radial stress ($\geq$16.9 MPa) on V_p is negligible. However, the performed CCS tests all showed higher velocities compared to the UCS experiments, implying more efficient compaction at confined conditions.

- CCS experiments conducted on an artificially, brine-saturated, fractured marble revealed that an increasing axial stress resulted in an increase in V_p whereas the fracture permeability decreased due to closure of its aperture. An increasing pore pressure showed the opposite effect: rising fracture permeability, due to its opening, and a decreasing V_p as the forces that act on grain contact surfaces reduced.

- Experimental observations for the brine-saturated fractured marble revealed that V_s is more sensitive to changes in pore pressure than V_p. On the other hand, V_s is less affected by an increasing axial stress compared to V_p. This resulted in V_s to slightly decrease, as a function of increasing axial stress ($\geq$ 27 MPa) and pore pressure ($\geq$ 11 MPa), whereas V_p tends to increase, for all temperatures studied.

- The combined temperature, axial stress, and pore pressure effect on both V_p and V_s was analysed by conducting multiple nonlinear regression on a large experimental dataset. It led to second-degree polynomial trends that could potentially be used for predicting seismic velocities at the Kızıldere, or other similar, geothermal site (s).

- For distinguishing between a 100% brine-saturated versus a fully supercritical CO_2-saturated fracture, the arrival times of the first arrivals were too close to each other to allow their utilization. The fracture aperture was too small compared to the wavelength of the source signal. However, visible differences in the amplitudes of the first arrivals were observed. The supercritical CO_2-saturated crack revealed consistently lower peak and trough amplitudes compared to the fully brine-saturated fracture, for both the P- and S-wave recordings.

CRediT authorship contribution statement

Martijn T.G. Janssen: Conceptualization, Methodology, Formal analysis, Investigation, Writing – original draft, Writing – review & editing, Visualization. **Deyan Draganov:** Conceptualization, Methodology, Supervision. **Auke Barnhoorn:** Conceptualization, Methodology, Supervision. **Karl-Heinz A.A. Wolf:** Conceptualization, Methodology, Supervision, Project administration, Funding acquisition.

Declaration of Competing Interest

The authors declare that they have no known competing financial interests or personal relationships that could have appeared to influence the work reported in this paper.

Data availability

Data will be made available on request.

Acknowledgments

References

Akın, S., Örücü, Y., Frıdrıksson, T., 2020. Characterizing the declining CO_2 emissions from Turkish geothermal power plants. In: Proceedings of the 45th Workshop on Geothermal Reservoir Engineering. Stanford University, USA, 10-12 February.

Araújo, R.G.S., Sousa, J.L.A.O., Bloch, M., 1997. Experimental investigation on the influence of temperature on the mechanical properties of reservoir rocks. Int. J. Rock Mech. Min. Sci. 34 (3–4), 298–2e1.

Barbier, E., 2002. Geothermal energy technology and current status: an overview. Renew. Sustain. Energy Rev. 6 (1–2), 3–65.

Barnhoorn, A., Verheij, J., Frehner, M., Zhubayev, A., Houben, M., 2018. Experimental identification of the transition from elasticity to inelasticity from ultrasonic attenuation analyses and the onset of inelasticity. Geophysics 83 (4), 221–229.

Berryman, J.G., 2005. Pore fluid effects on shear modulus in a model of heterogeneous rocks, reservoirs, and granular media. J. Geophys. Res. Solid Earth 110 (B7).

Bonnelye, A., Schubnel, A., David, C., Henry, P., Guglielmi, Y., Gout, C., Fauchille, A.L., Dick, P., 2017. Elastic wave velocity evolution of shales deformed under uppermost crustal conditions. J. Geophys. Res. Solid Earth 122 (1), 130–141.

Brown, S.R., 1987. Fluid flow through rock joints: the effect of surface roughness. J. Geophys. Res. Solid Earth 92 (B2), 1337–1347.

Bustaffa, E., Cori, L., Manzella, A., Nuvolone, D., Minichilli, F., Bianchi, F., Gorini, F., 2020. The health of communities living in proximity of geothermal plants generating heat and electricity: a review. Sci. Total Environ. 706, 135998.

Carman, P.C., 1937. Fluid flow through granular beds. Trans. Inst. Chem. Eng. 15, 150–166.

Chadwick, R.A., Williams, G.A., Falcon-Suarez, I., 2019. Forensic mapping of seismic velocity heterogeneity in a CO_2 layer at the Sleipner CO_2 storage operation, North Sea, using time-lapse seismics. Int. J. Greenh. Gas Control 90, 102793.

Christensen, N.I., Wang, H.F., 1985. The influence of pore pressure and confining pressure on dynamic elastic properties of Berea Sandstone. Geophysics 50 (2), 207–213.

Çiftçi, N.B., 2013. *In-situ* stress field and mechanics of fault reactivation in the gediz graben, Western Turkey. J. Geodyn. 65, 136–147.

Coskun, S.B., Wardlaw, N.C., 1993. Estimation of permeability from image analysis of reservoir sandstones. J. Pet. Sci. Eng. 10 (1), 1–16.

Darcy, H., 1856. Les Fontaines Publiques De La Ville De Dijon: Exposition Et Application. Victor Dalmont.

Darot, M., Reuschlé, T., 2000. Acoustic wave velocity and permeability evolution during pressure cycles on a thermally cracked granite. Int. J. Rock Mech. Min. Sci. 37 (7), 1019–1026.

Dwivedi, R.D., Goel, R.K., Prasad, V.V.R., Sinha, A., 2008. Thermo-mechanical properties of Indian and other granites. Int. J. Rock Mech. Min. Sci. 45 (3), 303–315.

Ekanem, A.M., Li, X.Y., Chapman, M., Main, I.G., 2016. Effects of CO_2 on P-wave attenuation in porous media with micro-cracks: a synthetic modelling study. J. Appl. Geophys. 135, 309–316.

El-Dessouky, H.T., Ettouney, H.M., 2002. Fundamentals of Salt Water Desalination. Elsevier.

Furre, A., 2002. The effective stress coefficient for wave velocities in saturated grain packs. In: Proceedings of the 64th EAGE Conference. Florence, Italy, 27-30 May.

Garg, S.K., Haizlip, J., Bloomfield, K.K., Kindap, A., Haklidir, F.S., Guney, A., 2015. A numerical model of the kizildere geothermal field, Turkey. In: Proceedings of the World Geothermal Congress. Melbourne, Australia, 19-25 April.

Ghosh, R., Sen, M.K., 2012. Predicting subsurface CO_2 movement: from laboratory to field scale. Geophysics 77 (3), 27–37.

Gokcen, G., Ozturk, H.K., Hepbasli, A., 2004. Overview of Kizildere geothermal power plant in Turkey. Energy Convers. Manag. 45 (1), 83–98.

Goos, E., Riedel, U., Zhao, L., Blum, L., 2011. Phase diagrams of CO_2 and CO_2–N_2 gas mixtures and their application in compression processes. Energy Procedia 4, 3778–3785.

Güleç, N., Hilton, D.R., 2016. Turkish geothermal fields as natural analogues of CO_2 storage sites: gas geochemistry and implications for CO_2 trapping mechanisms. Geothermics 64, 96–110.

Halaçoğlu, U., Fishman, M., Karaağaç, U., Harvey, W., Enerji, Z., 2018. Four decades of service— Kızıldere reservoir, units and management. GRC Trans. 42.

Heap, M.J., Mollo, S., Vinciguerra, S., Lavallée, Y., Hess, K.U., Dingwell, D.B., Baud, P., Iezzi, G., 2013. Thermal weakening of the carbonate basement under Mt. Etna volcano (Italy): implications for volcano instability. J. Volcanol. Geotherm. Res. 250, 42–60.

Hornby, B.E., 1996. An experimental investigation of effective stress principles for sedimentary rocks. In: Proceedings of the 66th SEG Annual Meeting. Denver, USA, 10-15 November 1996.

Hudson, J.A., Liu, E., 1999. Effective elastic properties of heavily faulted structures. Geophysics 64 (2), 479–485.

International Energy Agency (2021), World energy outlook 2021, IEA, . Licence: creative commons attribution CC BY-NC-SA 3.0 IGO.

Janssen, M.T.G. 2018. Seismic response of unconsolidated reservoirs as function of gas saturation (Shallow Gas: rock Physics and AVO) (Master's thesis).

Janssen, M.T.G., Barnhoorn, A., Draganov, D., Wolf, K.H.A., Durucan, S., 2021. Seismic velocity characterisation of geothermal reservoir rocks for CO₂ storage performance assessment. Appl. Sci. 11 (8), 3641.

Jaya, M.S., Shapiro, S.A., Kristinsdóttir, L.H., Bruhn, D., Milsch, H., Spangenberg, E., 2010. Temperature dependence of seismic properties in geothermal rocks at reservoir conditions. Geothermics 39 (1), 115–123.

Kaygusuz, K., Guney, M.S., Kaygusuz, O., 2019. Renewable energy for rural development in Turkey. J. Eng. Res. Appl. Sci. 8 (1), 1109–1118.

Kern, H., 1978. The effect of high temperature and high confining pressure on compressional wave velocities in quartz-bearing and quartz-free igneous and metamorphic rocks. Tectonophysics 44 (1–4), 185–203.

Kern, H., Popp, T., Gorbatsevich, F., Zharikov, A., Lobanov, K.V., Smirnov, Y.P., 2001. Pressure and temperature dependence of VP and VS in rocks from the superdeep well and from surface analogues at Kola and the nature of velocity anisotropy. Tectonophysics 338 (2), 113–134.

Kestin, J., Khalifa, H.E., Correia, R.J., 1981. Tables of the dynamic and kinematic viscosity of aqueous NaCl solutions in the temperature range 20–150 C and the pressure range 0.1–35MPa. J. Phys. Chem. Ref. Data 10 (1), 71–88.

King, M.S., 2009. Recent developments in seismic rock physics. Int. J. Rock Mech. Min. Sci. 46 (8), 1341–1348.

Kozeny, J., 1927. Ueber kapillare leitung der wassers im Boden. Sitzungsberichte Akademie der Wissenschaften in Wien 136, 271–306.

Kristinsdóttir, L.H., Flóvenz, Ó.G., Árnason, K., Bruhn, D., Milsch, H., Spangenberg, E., Kulenkampff, J., 2010. Electrical conductivity and P-wave velocity in rock samples from high- temperature Icelandic geothermal fields. Geothermics 39 (1), 94–105.

Lavrov, A., 2017. Fracture permeability under normal stress: a fully computational approach. J. Pet. Explor. Prod. Technol. 7 (1), 181–194.

Liu, E., Tod, S.R., Li, X.Y., 2002. Effects of stress and pore fluid pressure on seismic anisotropy in cracked rock. CSEG Rec. 27 (6), 92–98.

Liu, W., Zhang, L., Luo, N., 2020. Elastic modulus evolution of rocks under heating–cooling cycles. Sci. Rep. 10 (1), 1–9.

Mavko, G., Jizba, D., 1991. Estimating grain-scale fluid effects on velocity dispersion in rocks. Geophysics 56 (12), 1940–1949.

Mavko, G., Mukerji, T., 1998. Bounds on low-frequency seismic velocities in partially saturated rocks. Geophysics 63 (3), 918–924.

Mavko, G., Mukerji, T., Dvorkin, J., 2020. The Rock Physics Handbook. Cambridge university press.

Muralidharan, V., Chakravarthy, D., Putra, E., Schechter, D.S., 2004. Investigating fracture aperture distributions under various stress conditions using X-ray CT scanner. In: Proceedings of the 5th Canadian International Petroleum Conference. Calgary, Canada, 8-10 June.

Njiekak, G., Schmitt, D.R., Yam, H., Kofman, R.S., 2013. CO₂ rock physics as part of the Weyburn- Midale geological storage project. Int. J. Greenh. Gas Control 16, 118–133.

Nur, A., Simmons, G., 1969. The effect of saturation on velocity in low porosity rocks. Earth Planet. Sci. Lett. 7 (2), 183–193.

Ozcelik, M., 2022. Environmental and social impacts of the increasing number of geothermal power plants (Büyük Menderes Graben—Turkey). Environ. Sci. Pollut. Res. 29 (11), 15526–15538.

Parlaktuna, M., Durucan, Ş., Parlaktuna, B., Sinayuç, Ç., Janssen, M.T.G., Şentürk, E., Tonguc, E., Demircioglu, Ö., Poletto, F., Böhm, G., Bellezza, C., 2021. Seismic velocity characterisation and survey design to assess CO₂ injection performance at Kızıldere geothermal field. Turk. J. Earth Sci. 30 (SI–2), 1061–1075.

Pavese, A., Catti, M., Parker, S.C., Wall, A., 1996. Modelling of the thermal dependence of structural and elastic properties of calcite, CaCO₃. Phys. Chem. Miner. 23 (2), 89–93.

Pellet, F.L., Fabre, G., 2007. Damage evaluation with P-wave velocity measurements during uniaxial compression tests on argillaceous rocks. Int. J. Geomech. 7 (6), 431–436.

Podio-Lucioni, A., 1968. Experimental Determination of the Dynamic Elastic Properties of Anisotropic rocks, Ultrasonic Pulse Method. The University of Texas at Austin. Ph. D thesis.

Pokrovsky, O.S., Golubev, S.V., Schott, J., Castillo, A., 2009. Calcite, dolomite and magnesite dissolution kinetics in aqueous solutions at acid to circumneutral pH, 25 to 150°C and 1 to 55 atm pCO₂: new constraints on CO₂ sequestration in sedimentary basins. Chem. Geol. 265 (1–2), 20–32.

Potter, J.M., Brown, D.L., 1977. The volumetric properties of aqueous sodium chloride solutions. US Geol. Surv. Bull.

Prasad, M., Manghnani, M.H., 1997. Effects of pore and differential pressure on compressional wave velocity and quality factor in Berea and Michigan sandstones. Geophysics 62 (4), 1163–1176.

Punturo, R., Kern, H., Cirrincione, R., Mazzoleni, P., Pezzino, A., 2005. P-and S-wave velocities and densities in silicate and calcite rocks from the Peloritani Mountains, Sicily (Italy): the effect of pressure, temperature and the direction of wave propagation. Tectonophysics 409 (1– 4), 55–72.

Qi, H., Ba, J., Müller, T.M., 2021. Temperature effect on the velocity-porosity relationship in rocks. J. Geophys. Res. Solid Earth 126 (1) e2019JB019317.

Robertson, J.D., Nogami, H.H., 1984. Complex seismic trace analysis of thin beds. Geophysics 49 (4), 344–352.

Scheu, B., Kern, H., Spieler, O., Dingwell, D.B., 2006. Temperature dependence of elastic P-and S- wave velocities in porous Mt. Unzen dacite. J. Volcanol. Geotherm. Res. 153 (1–2), 136–147.

Shi, J.Q., Xue, Z., Durucan, S., 2007. Seismic monitoring and modelling of supercritical CO₂ injection into a water-saturated sandstone: interpretation of P-wave velocity data. Int. J. Greenh. Gas Control 1 (4), 473–480.

Soltani, M., Kashkooli, F.M., Souri, M., Rafiei, B., Jabarifar, M., Gharali, K., Nathwani, J. S., 2021. Environmental, economic, and social impacts of geothermal energy systems. Renew. Sustain. Energy Rev. 140, 110750.

Tang, Z.C., Sun, M., Peng, J., 2019. Influence of high temperature duration on physical, thermal and mechanical properties of a fine-grained marble. Appl. Therm. Eng. 156, 34–50.

Thorbecke, J.W., Draganov, D., 2011. Finite-difference modelling experiments for seismic interferometry. Geophysics 76 (6), H1–H18.

Timur, A., 1977. Temperature dependence of compressional and shear wave velocities in rocks. Geophysics 42 (5), 950–956.

Török, A., Török, Á., 2015. The effect of temperature on the strength of two different granites. Cent. Eur. Geol. 58 (4), 356–369.

Vagnon, F., Colombero, C., Colombo, F., Comina, C., Ferrero, A.M., Mandrone, G., Vinciguerra, S.C., 2019. Effects of thermal treatment on physical and mechanical properties of Valdieri Marble-NW Italy. Int. J. Rock Mech. Min. Sci. 116, 75–86.

Wang, X.Q., Schubnel, A., Fortin, J., David, E.C., Guéguen, Y., Ge, H.K., 2012. High Vp/Vs ratio: saturated cracks or anisotropy effects? Geophys. Res. Lett. 39 (11).

Wyllie, M.R.J., Gregory, A.R., Gardner, G.H.F., 1958. An experimental investigation of factors affecting elastic wave velocities in porous media. Geophysics 23 (3), 459–493.

Xu, X., Hofmann, R., Batzle, M., Tshering, T., 2006. Influence of pore pressure on velocity in low- porosity sandstone: implications for time-lapse feasibility and pore-pressure study. Geophys. Prospect. 54 (5), 565–573.

Yamanlar, S., Korkmaz, E.D., Serpen, U., 2020. Assessment of geothermal power potential in Buyuk Menderes Basin, Turkey. Geothermics 88, 101912.

Yavuz, H., Demirdag, S., Caran, S., 2010. Thermal effect on the physical properties of carbonate rocks. Int. J. Rock Mech. Min. Sci. 47 (1), 94–103.

Zohuri, B., 2020. Nuclear Fuel Cycle and Decommissioning. In Nuclear Reactor Technology Development and Utilization. Woodhead Publishing, pp. 61–120.